
Witnessing Adversarial Training in Reproducing Kernel Hilbert Spaces

Arash Mehrjou^{1,2} Wittawat Jitkrittum¹ Bernhard Schölkopf¹ Krikamol Muandet¹

Abstract

Modern implicit generative models such as generative adversarial networks (GANs) are generally known to suffer from instability and lack of interpretability as it is difficult to diagnose what aspects of the target distribution are missed by the generative model. In this work, we propose a theoretically grounded solution to these issues by augmenting the GAN’s loss function with a kernel-based regularization term that magnifies local discrepancy between the distributions of generated and real samples. The proposed method relies on so-called witness points in the data space which are jointly trained with the generator and provide an interpretable indication of where the two distributions locally differ during the training procedure. In addition, the proposed algorithm is scaled to higher dimensions by learning the witness locations in a latent space of an autoencoder. We theoretically investigate the dynamics of the training procedure, prove that a desirable equilibrium point exists, and the dynamical system is locally stable around this equilibrium. Finally, we demonstrate different aspects of the proposed algorithm by numerical simulations of analytical solutions and empirical results for low and high-dimensional datasets.

1. Introduction

Recent success of generative adversarial networks (GANs) (Goodfellow et al., 2014) and its eye-catching results in various applications (Karras et al., 2018; Zhu et al., 2017; Li et al., 2017b; Mehrjou et al., 2018) have inspired many machine learning algorithms whose objective is a game between two or more players. GANs have been widely studied in the past few years from different perspectives

¹Max Planck Institute for Intelligent Systems, Tübingen, Germany ²Max Planck ETH Center for Learning Systems, Zürich, Switzerland. Correspondence to: Arash Mehrjou <amehrjou@tuebingen.mpg.de>.

Submitted to the 35th International Conference on Machine Learning, Stockholm, Sweden, PMLR 80, 2018. Copyright 2018 by the author(s).

such as information theory (Chen et al., 2016), dynamical systems (Nagarajan & Kolter, 2017; Mehrjou & Schölkopf, 2018), and game theory (Daskalakis et al., 2018).

Despite the practical successes, GANs have suffered from lack of theoretical understanding of what is actually learned by the generator and how close the distribution of generated samples is to the real one (Arora et al., 2018). Moreover, the instability of training GANs and its reliance on immense hyper-parameter tuning also remains a major issue. On the other hand, classical generative algorithms especially those based on kernel methods are well understood for years but their performance have not been comparable with GANs (Li et al., 2015; Dziugaite et al., 2015). This brings us the possibility of combining ideas of modern and classical methods to have the best of both worlds (Li et al., 2017a).

Recent studies have suggested that some kernel-based algorithms for training GANs are stable (Nagarajan & Kolter, 2017; Wang et al., 2019) and several ideas have been proposed to improve the algorithms (Sutherland et al., 2017; Li et al., 2017a; Bińkowski et al., 2018; Arbel et al., 2018). A notable analysis is performed through the lens of dynamical systems (Wilson et al., 2016; Sertl & Dellnitz, 2006; Schropp & Singer, 2000) to gain insight into the dynamics of GANs. The dynamical system becomes even more challenging in saddle point problems when the properties of an equilibrium correlate with the quality of the solution, e.g., in GANs (Mescheder et al., 2018; Nagarajan & Kolter, 2017; Mehrjou et al., 2017) and non-cooperative games (Smale, 1980). Similar analysis can also be extended to more generic scenarios when multiple players are engaged in a dynamical game (Balduzzi et al., 2018).

In this work, we propose a generic game with new players called *witness points* (Chwialkowski et al., 2015; Jitkrittum et al., 2016) which can be combined with several objectives of implicit generative models. This combination provides an explicit trade-off between *global* and *local* differences between the real and generated distributions (see Fig. 1). In addition to theoretical motivations for these players, they provably give rise to better convergence of the algorithm. Witness points also improve the interpretability of the models as they can be seen as a set of probes that are planted inside the learning machine allowing us to read out the current state of the algorithm. As a result, this gives a better

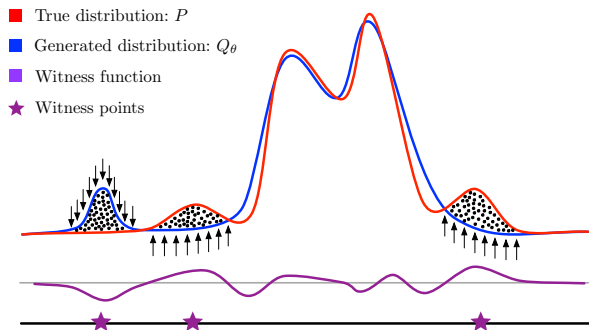


Figure 1. While most of the existing objectives can capture the *global* discrepancy between the true distribution and the synthetic one, optimizing over the witness points proposed in this work allows us to locate the *local* differences between the two distributions. The witness points who have detected the local differences guide the probability mass of the model to capture the missed regions (as shown by arrows).

understanding of the distribution being learned or missed by the generator. We also extend the idea of witness points to an abstract low-dimensional space, i.e., the latent space, associated with an autoencoder to deal with high-dimensional data (Section 3.3). Lastly, we support our idea with theoretical analysis from the perspective of dynamical systems (Section 3.5).

The remaining of this paper is organized as follows. First, we review the background material in Section 2. We then introduce the proposed method in Section 3. Our theoretical analyses are presented in Section 3.5, followed by the simulation and empirical results in Section 4. Finally, we present the discussion on related works in Section 5.

2. Background

Generative adversarial networks are among the most popular techniques for learning a high-dimensional generative model (Goodfellow et al., 2014). The idea is based on an adversarial game between two players, namely, a *generator* and a *discriminator*. Let \mathcal{Z} and \mathcal{X} be latent space and data space, respectively. The generator $G_\theta : \mathcal{Z} \rightarrow \mathcal{X}$ is defined via a generative process $\mathbf{y} = G_\theta(\mathbf{z})$ for $\mathbf{z} \sim P_{\mathcal{Z}}$ where G_θ is usually a feedforward neural network parameterized by θ and $P_{\mathcal{Z}}$ is a simple distribution over the latent space, e.g., $P_{\mathcal{Z}} = \mathcal{N}(\mathbf{0}, \mathbf{I})$ for $\mathcal{Z} = \mathbb{R}^{d_z}$. Hence, it is easy to sample from G_θ as it involves only one forward pass through the generator network. The discriminator $D : \mathcal{X} \rightarrow \mathbb{R}$ takes a data point \mathbf{x} as an input and then outputs a score $D(\mathbf{x})$, e.g., via a classifier $D : \mathcal{X} \rightarrow [0, 1]$.

Given a dataset $D = \{\mathbf{x}_1, \dots, \mathbf{x}_n\}$ of i.i.d. samples from $P_{\mathcal{X}}$, the vanilla GAN (Goodfellow et al., 2014) learns the generator G_θ to approximate $P_{\mathcal{X}}$ by solving the following

minimax optimization problem:

$$\min_G \max_D \mathbb{E}_{\mathbf{x}}[\log D(\mathbf{x})] + \mathbb{E}_{\mathbf{z}}[\log(1 - D(G(\mathbf{z})))].$$

Let $Q_{\mathcal{Y}}$ be the distribution induced by the generator G_θ . Then, it was shown that the above problem is equivalent to minimizing the Jensen-Shannon (JS) divergence between $P_{\mathcal{X}}$ and $Q_{\mathcal{Y}}$ (Goodfellow et al., 2014) which was later extended to more generic distances (Nowozin et al., 2016).

2.1. Maximum Mean Discrepancy

In this work we focus on a maximum mean discrepancy (MMD) as discrepancy measure between $P_{\mathcal{X}}$ and $Q_{\mathcal{Y}}$ (Gretton et al., 2012). Let \mathcal{F} be a reproducing kernel Hilbert space (RKHS) defined by the positive definite kernel $k: \mathcal{X} \times \mathcal{X} \rightarrow \mathbb{R}$ with the canonical feature map $\phi: \mathcal{X} \rightarrow \mathcal{F}$ i.e., $\phi(\mathbf{x}) := k(\mathbf{x}, \cdot)$ and $k(\mathbf{x}, \mathbf{y}) = \langle \phi(\mathbf{x}), \phi(\mathbf{y}) \rangle_{\mathcal{F}}$ for all $\mathbf{x}, \mathbf{y} \in \mathcal{X}$. The MMD between $P_{\mathcal{X}}$ and $Q_{\mathcal{Y}}$ can be defined as

$$\begin{aligned} \text{MMD}^2(P, Q) &= \sup_{f \in \mathcal{F}, \|f\| \leq 1} \left| \int f dP_{\mathcal{X}} - \int f dQ_{\mathcal{Y}} \right| \\ &= \|\mu_{P_{\mathcal{X}}} - \mu_{Q_{\mathcal{Y}}}\|_{\mathcal{F}}^2, \end{aligned} \quad (1)$$

where $\mu_{P_{\mathcal{X}}} := \mathbb{E}_{\mathbf{x} \sim P_{\mathcal{X}}}[k(\mathbf{x}, \cdot)]$ and $\mu_{Q_{\mathcal{Y}}} := \mathbb{E}_{\mathbf{y} \sim Q_{\mathcal{Y}}}[k(\mathbf{y}, \cdot)]$ are the so-called mean embeddings of $P_{\mathcal{X}}$ and $Q_{\mathcal{Y}}$ (Muandet et al., 2017). For a characteristic kernel k (Fukumizu et al., 2008; Gretton et al., 2012), $\text{MMD}^2(P, Q) = 0$ if and only if $P_{\mathcal{X}} = Q_{\mathcal{Y}}$, i.e., the MMD is a proper metric on a space of distributions. It is instructive to note that the MMD can be viewed as an integral probability metric (IPM) whose function class is a unit ball in the RKHS associated with the kernel k (Müller, 1997; Nowozin et al., 2016; Arjovsky et al., 2017). In the following, we discuss briefly how MMD has been used in generative models to prepare for the presentation of our proposed method in Section 3.

MMD-GAN. Dziugaite et al. (2015) and Li et al. (2015) first proposed to learn a generator $Q_{\mathcal{Y}} = G_\theta(\mathbf{Z})$ so as to minimize $\text{MMD}^2(P_{\mathcal{X}}, Q_{\mathcal{Y}})$ w.r.t. θ . Since the discriminator lives in a unit ball of the RKHS, the benefit of this formulation is that the maximization problem w.r.t. the discriminator can be solved analytically, as seen from (1). In higher dimensions, however, the MMD-GAN usually produces a generator that is inferior to those produced by other variants of GANs. Hence, several methods have been proposed recently to the MMD-GAN including optimized kernels and feature extractors (Sutherland et al., 2017; Li et al., 2017a), gradient regularization (Bińkowski et al., 2018; Arbel et al., 2018), and repulsive loss (Wang et al., 2019), to enumerate a few examples.

3. Proposed Method

Our idea is to construct a set of points $\mathbb{V} = \{v_1, \dots, v_J\} \subset \mathcal{V}$, which we call *witness points*, whose role is to capture *local* differences between the real distribution $P_{\mathbf{X}}$ and the generated one $Q_{\mathbf{Y}}$ and to provide an interpretable tool for model diagnosis.

3.1. Discrepancy Measure via Witness Points

We can rewrite the MMD (1) as $\|\mathbf{w}\|_{\mathcal{F}}^2$ where $\mathbf{w} := \mu_{P_{\mathbf{X}}} - \mu_{Q_{\mathbf{Y}}} \in \mathcal{F}$ is known as a witness function which characterizes the differences between $P_{\mathbf{X}}$ and $Q_{\mathbf{Y}}$ (see an illustration in Fig. 1). For any $\mathbf{x} \in \mathcal{X}$, let $\mathbf{w}(\mathbf{x})$ be a witness function evaluation at \mathbf{x} which, according to the reproducing property of \mathcal{F} , can be computed by

$$\mathbf{w}(\mathbf{x}) = \langle \mu_{P_{\mathbf{X}}} - \mu_{Q_{\mathbf{Y}}}, \phi(\mathbf{x}) \rangle_{\mathcal{F}} = \mu_{P_{\mathbf{X}}}(\mathbf{x}) - \mu_{Q_{\mathbf{Y}}}(\mathbf{x}).$$

By projecting the witness function \mathbf{w} onto a set of J directions $\{\phi(v_1), \dots, \phi(v_J)\}$ in the RKHS \mathcal{F} , Chwialkowski et al. (2015) and Jitkrittum et al. (2016) propose a discrepancy measure that is the Euclidean distance computed w.r.t. the projected values, i.e.,

$$\begin{aligned} \text{UME}^2 &= \frac{1}{J} \left\| \begin{pmatrix} \mu_{P_{\mathbf{X}}}(v_1) \\ \vdots \\ \mu_{P_{\mathbf{X}}}(v_J) \end{pmatrix} - \begin{pmatrix} \mu_{Q_{\mathbf{Y}}}(v_1) \\ \vdots \\ \mu_{Q_{\mathbf{Y}}}(v_J) \end{pmatrix} \right\|_2^2 \\ &= \frac{1}{J} \sum_{j=1}^J (\mu_{P_{\mathbf{X}}}(v_j) - \mu_{Q_{\mathbf{Y}}}(v_j))^2. \end{aligned} \quad (2)$$

This is known as the *unnormalized mean embeddings* (UME) statistic. Chwialkowski et al. (2015) shows that if k is characteristic, translation invariant, real analytic, and $\{v_j\}_{j=1}^J$ are drawn from any distribution η with a density, then for any $J \geq 1$, η -almost surely, $\text{ME}^2(P_{\mathbf{X}}, Q_{\mathbf{Y}}) = 0$ if and only if $P_{\mathbf{X}} = Q_{\mathbf{Y}}$. Jitkrittum et al. (2016) further extends the statistic by proposing optimizing $\{v_j\}_{j=1}^J$ so as to maximize the test power of the two-sample test proposing $H_0: P_{\mathbf{X}} = Q_{\mathbf{Y}}$ against $H_1: P_{\mathbf{X}} \neq Q_{\mathbf{Y}}$. The result is an interpretable two-sample test which gives an evidence in the form of optimized witness points showing where $P_{\mathbf{X}}$ and $Q_{\mathbf{Y}}$ differ most (in the domain $\mathcal{X} \cup \mathcal{Y}$).

3.2. Our Objective

Based on J witness points in \mathcal{X} , we propose to learn the generator G_{θ} by solving

$$\min_{\theta} \max_{\{v_j\}_{j=1}^J} \mathcal{L}_{\lambda}(\theta, \{v_j\}_{j=1}^J), \quad (3)$$

where the loss function is defined as

$$\mathcal{L}_{\lambda}(\theta, \mathbb{V}) := \mathcal{D}(P_{\mathbf{X}}, Q_{\mathbf{Y}}) + \lambda \cdot \text{UME}^2(P_{\mathbf{X}}, Q_{\mathbf{Y}}, \mathbb{V}). \quad (4)$$

Here, $\mathcal{D}(P_{\mathbf{X}}, Q_{\mathbf{Y}})$ is an arbitrary GAN objective and $\lambda > 0$ is a trade-off parameter. The empirical estimate of (4) can be obtained using the observations $\mathbf{x}_1, \dots, \mathbf{x}_n$ from $P_{\mathbf{X}}$ and the generated samples $\mathbf{y}_1, \dots, \mathbf{y}_m$ from the generator $Q_{\mathbf{Y}} = G_{\theta}$ as

$$\begin{aligned} \widehat{\mathcal{L}}_{\lambda}(\theta, \mathbb{V}) &= \mathcal{D}(\widehat{P}_{\mathbf{X}}, \widehat{Q}_{\mathbf{Y}}) \\ &+ \frac{\lambda}{J} \sum_{j=1}^J \left(\frac{1}{n} \sum_{i=1}^n k(\mathbf{x}_i, v_j) - \frac{1}{m} \sum_{j=1}^m k(\mathbf{y}_j, v_j) \right)^2 \end{aligned} \quad (5)$$

where $\widehat{P}_{\mathbf{X}} := \frac{1}{n} \sum_{i=1}^n \delta_{\mathbf{x}_i}$ and $\widehat{Q}_{\mathbf{Y}} := \frac{1}{m} \sum_{j=1}^m \delta_{\mathbf{y}_j}$ denote the empirical distributions.

It can be observed that (i) the first term on the rhs of (4) acts as a *global* discrepancy measure between $P_{\mathbf{X}}$ and $Q_{\mathbf{Y}}$. For example, one may consider $\mathcal{D}(P_{\mathbf{X}}, Q_{\mathbf{Y}}) = \text{MMD}^2(P_{\mathbf{X}}, Q_{\mathbf{Y}})$, i.e., the objective used in the MMD-GAN, (ii) the second term acts as an auxiliary objective that provides us with a *local* discrepancy measure between $P_{\mathbf{X}}$ and $Q_{\mathbf{Y}}$. This allows the generator to learn the fine details of the data, (iii) and by maximizing $\text{UME}^2(P_{\mathbf{X}}, Q_{\mathbf{Y}}, \{v_j\}_{j=1}^J)$ at each iteration w.r.t. the witness points $\{v_j\}_{j=1}^J$, the witness points tell us where $P_{\mathbf{X}}$ and $Q_{\mathbf{Y}}$ differ most. Due to the reasons mentioned above, we name the proposed algorithm GLOCAD that stands for *GLO*bal/*LO*cal *Ad*aptive *Disc*rimination.

Example 1. Consider a special case when we have $\mathcal{D}(P_{\mathbf{X}}, Q_{\mathbf{Y}}) = \text{MMD}^2(P_{\mathbf{X}}, Q_{\mathbf{Y}})$ where $Q_{\mathbf{Y}} = G_{\theta}(\mathbf{Z})$. Then, our objective (4) can be expressed as

$$\mathcal{L}_{\lambda}(\theta, \{v_j\}_{j=1}^J) = \|\mathbf{w}_{\theta}\|_{\mathcal{F}}^2 + \frac{\lambda}{J} \sum_{j=1}^J \mathbf{w}_{\theta}(v_j)^2, \quad (6)$$

where $\mathbf{w}_{\theta} := \mu_{P_{\mathbf{X}}} - \mu_{Q_{\mathbf{Y}}}$ is a witness function. One can see from (6) that the objective function allows us to capture both local and global difference between $P_{\mathbf{X}}$ and $Q_{\mathbf{Y}}$ simultaneously. Note that each term in the sum above takes the form $\langle \mathbf{w}, \phi(v) \rangle_{\mathcal{F}}^2 = \langle \mathbf{w}, \phi(v) \rangle_{\mathcal{F}} \langle \phi(v), \mathbf{w} \rangle_{\mathcal{F}}$ so we can rewrite this as $\langle \mathbf{w}, C \mathbf{w} \rangle_{\mathcal{F}}$ where $C: \mathcal{F} \rightarrow \mathcal{F}$ is an operator summing over rank-1 operators. We discuss this interpretation further in Appendix ??

The training algorithm interlaces training iterations over the local term $\text{UME}^2(P_{\mathbf{X}}, Q_{\mathbf{Y}}, \{v_j\}_{j=1}^J)$ (w.r.t. witness points) with training iterations of the the total loss $\mathcal{L}_{\lambda}(\theta, \{v_j\}_{j=1}^J)$ (w.r.t. the parameters of the generator). The number of iterations by which each term is updated are left as hyper-parameters. See Alg. 1 for more details.

3.3. GLOCAD in Latent Space

Alg. 1, in essence, places witness points in the same space as the data. This works well when the differences between

Algorithm 1 GLOCAD

input : J the number of witness points, λ the weight of the UME term, γ the learning rate, B the batch size, n_g, n_v the number of iterations to optimize the generator and the witness points in each loop.
 do initialize generator and discriminator parameters $\{\theta_g, \theta_d\}$; initialize witness points $\mathbb{V}_0 = \{v_j(0)\}_{j=1}^J$; define the convergence criterion;
output : the generator function $G_{\theta_g}(z)$ and witness points $\mathbb{V} = \{v_j\}_{j=1}^J$.

while convergence criterion is not met **do**

for $t = 1, \dots, n_v$ **do**

Sample minibatches $\mathbb{X} = \{\mathbf{x}_i\}_{i=1}^B \sim P_{\mathbf{X}}$ and $\mathbb{Z} = \{\mathbf{z}_j\}_{j=1}^B \sim P_{\mathbf{Z}}$

for $j = 1, \dots, J$ **do**

$\mathbf{v}_j \leftarrow \mathbf{v}_j + \gamma \cdot \nabla_{\mathbf{v}_j} \mathcal{L}_\lambda(\theta_g, \mathbb{V})$

for $t = 1, \dots, n_g$ **do**

Sample minibatches \mathbb{X} and \mathbb{Z}

$\theta_g \leftarrow \theta_g - \gamma \cdot \nabla_{\theta_g} \mathcal{L}_\lambda(\theta_g, \mathbb{V})$

the two distributions can be localized in the data space. However, when the data space is complex (e.g., natural images), localizing the differences in the original domain (e.g., pixel space) may not be effective, and it may become necessary to detect differences in another task-dependent transformed space (e.g., the feature space of images). To this end, we propose to augment Alg. 1 with extra components to improve its performance on natural data.

To deal with more complex data manifolds $\mathcal{M} = \text{supp}(P_{\mathbf{X}}) \subset \mathcal{X}$, we restrict the witness points $\{v_j\}_{j=1}^J$ to lie in the latent space \mathcal{L} of an autoencoder (Hinton & Salakhutdinov, 2006) where $\dim(\mathcal{L}) \ll \dim(\mathcal{X})$. Formally, we denote an autoencoder parameterized by $\theta_d = \{\theta_d^e, \theta_d^d\}$ as $A_{\theta_d} : \mathcal{X} \rightarrow \mathcal{X}$, consisting of an encoder $E_{\theta_d^e} : \mathcal{X} \rightarrow \mathcal{L}$ and a decoder $D_{\theta_d^d} : \mathcal{L} \rightarrow \mathcal{X}$ such that $A_{\theta_d}(\mathbf{x}) = D_{\theta_d^d}(E_{\theta_d^e}(\mathbf{x}))$. Fig. 2 depicts the overall schematic of the algorithm when the autoencoder is incorporated.

The new objective function can then be written as

$$\mathcal{L}(\theta_g, \theta_d, \mathbb{V}) = \mathcal{L}_{\lambda_1}(\theta_g, \mathbb{V}) + \lambda_2 \mathcal{L}^r(\theta_d^e, \theta_d^d), \quad (7)$$

where the first term on the rhs is equivalent to the original loss in (5) except that the kernel now depends on the encoder $E_{\theta_d^e}$, i.e., $k_{E_{\theta_d^e}}(\mathbf{x}, \mathbf{y}) = k(E_{\theta_d^e}(\mathbf{x}), E_{\theta_d^e}(\mathbf{y}))$. The second term on the rhs measures the *reconstruction error* of the autoencoder A_{θ_d} and can be estimated by $\mathcal{L}^r(\theta_d^e, \theta_d^d) := \frac{1}{B} \sum_{i=1}^B \|\mathbf{x}_i - D_{\theta_d^d}(E_{\theta_d^e}(\mathbf{x}_i))\|_2^2 + \frac{1}{B} \sum_{i=1}^B \|G_{\theta_g}(\mathbf{z}_i) - D_{\theta_d^d}(E_{\theta_d^e}(G_{\theta_g}(\mathbf{z}_i)))\|_2^2$ when applied to the observations

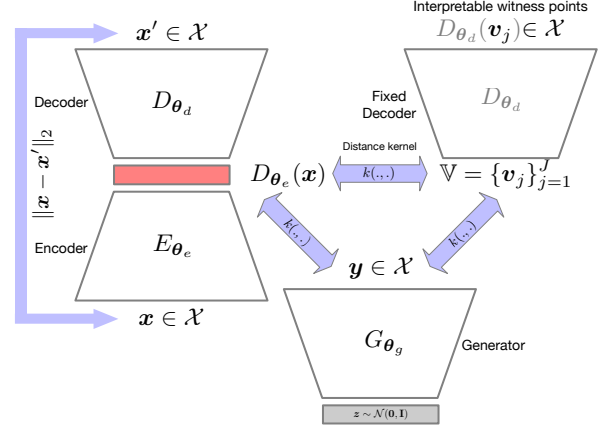


Figure 2. The schematic of Auto-GLOCAD where the witness points v_j live in the code space. The trained decoder is used to visualize the witness points.

$\{\mathbf{x}_1, \dots, \mathbf{x}_B\} \cup \{\mathbf{z}_1, \dots, \mathbf{z}_B\}$ in a minibatch of size $2B$.

The benefits of our new objective (7) are threefold. First, the witness points now live in the latent space \mathcal{L} of the autoencoder which is of lower dimension than the data space \mathcal{X} . Hence, the optimization problem w.r.t the witness points becomes more tractable. Second, the reconstruction loss encourages the encoder to be injective. Consequently, the encoder maps points from the data space to the input space of the kernel without a major loss of information, and allows the trained kernel to remain characteristic (Li et al., 2017a). Finally, the reconstruction loss also forces the decoder to provide meaningful reconstruction. Thus, we can obtain an interpretable visualization of the witness point v living in the abstract latent space \mathcal{L} to the corresponding point on the data manifold by $\tilde{\mathbf{x}} = D_{\theta_d^d}(v)$.

We call this version of the algorithm which is built on top of GLOCAD, Auto-GLOCAD due to the incorporated autoencoder architecture. See Alg. 2 for more details.

3.4. Adaptive Filter Interpretation

To elaborate more on the trade-off between the global and local terms in (6), we consider the shift-invariant kernel $k(\mathbf{x}, \mathbf{x}') = \psi(\mathbf{x} - \mathbf{x}')$ where $\mathbf{x}, \mathbf{x}' \in \mathbb{R}^{d_x}$ and ψ is a positive definite function. Let $\varphi_{P_{\mathbf{X}}}$ and $\varphi_{Q_{\mathbf{Y}}}$ be characteristic functions of $P_{\mathbf{X}}$ and $Q_{\mathbf{Y}}$, respectively. Using Bochner's theorem (Loomis, 2013) and the Euler's formula, we can rewrite (6) in the Fourier domain as

$$\int_{\mathbb{R}^{d_x}} |\varphi_{P_{\mathbf{X}}}(\omega) - \varphi_{Q_{\mathbf{Y}}}(\omega)|^2 d\Lambda(\omega) + \frac{\lambda}{J} \sum_{j=1}^J \left(\int_{\mathbb{R}^d} [\varphi_{P_{\mathbf{X}}}(\omega) - \varphi_{Q_{\mathbf{Y}}}(\omega)] \cos(\omega^\top v_j) d\Lambda(\omega) \right)^2,$$

Algorithm 2 Auto-GLOCAD

input : $J, \lambda, \gamma, c, B, n_g, n_v$ as Alg. 1 and n_e, n_d the training iterations for encoder and decoder.
 do initialization as Alg. 1; initialize encoder and decoder parameters θ_d^e, θ_d^d ; define the convergence criterion;
output : $G_{\theta_g}(z), \mathbb{V}$ as Alg. 1 and the decoder $D_{\theta_d}(\cdot)$.
while *convergence criterion is not met* **do**
 for $t = 1, \dots, n_d$ **do**
 Sample minibatches $\mathbb{X} = \{\mathbf{x}_i\}_{i=1}^B \sim P_{\mathbf{X}}$ and $\mathbb{Z} = \{\mathbf{z}_j\}_{j=1}^B \sim P_{\mathbf{Z}}$
 $\theta_d^e \leftarrow \theta_d^e - \gamma \cdot \nabla_{\theta_d^e} \mathcal{L}^r_{(\theta_d^e, \theta_d^d)}(\mathbb{X}, \mathbb{Z})$
 $\theta_d^d \leftarrow \theta_d^d - \gamma \cdot \nabla_{\theta_d^d} \mathcal{L}^r_{(\theta_d^e, \theta_d^d)}(\mathbb{X}, \mathbb{Z})$
 for $t = 1, \dots, n_e$ **do**
 Sample minibatches \mathbb{X} and \mathbb{Z}
 $\theta_d^e \leftarrow \theta_d^e + \gamma \cdot \nabla_{\theta_d^e} \mathcal{L}_{(\theta_d^e, \theta_g, \mathbb{V})}(\mathbb{X}, \mathbb{Z})$
 for $t = 1, \dots, n_g$ **do**
 Sample minibatches \mathbb{X} and \mathbb{Z}
 $\theta_g \leftarrow \theta_g - \gamma \cdot \nabla_{\theta_g} \mathcal{L}_{(\theta_d^e, \theta_g, \mathbb{V})}(\mathbb{X}, \mathbb{Z})$
 for $t = 1, \dots, n_v$ **do**
 Sample minibatches \mathbb{X} and \mathbb{Z}
 for $j = 1, \dots, J$ **do**
 $\mathbf{v}_j \leftarrow \mathbf{v}_j + \gamma \cdot \nabla_{\mathbf{v}_j} \mathcal{L}_{(\theta_d^e, \theta_g, \mathbb{V})}(\mathbb{X}, \mathbb{Z})$

where Λ is the inverse Fourier transform of the kernel k . As we can see, $\{\mathbf{v}_j\}_{j=1}^J$ appear as the frequency modulators. The summands of the second term are most sensitive to frequencies which are determined by witness points $\{\mathbf{v}_j\}_{j=1}^J$. Since these witness points are trainable, they determine frequencies to be learned at each iteration. For example, in the case of natural images, the algorithm has the freedom to first learn the low frequency (long-range) structure of the image and then shift its attention to learning the high frequency fine details. This transition is adaptively controlled by witness points $\{\mathbf{v}_j\}_{j=1}^J$. An experiment will be presented to empirically show this interpretation in Section 4 and Fig. 6. Another interpretation is viewing the witness points as the axes of a trainable coordinate system. The gradients are scaled by a change-of-coordinate matrix at every iteration. Further details on this interpretation can be found in Section C of the appendix.

3.5. Stability Analysis

In this section, we explore theoretical aspects of our algorithm from the perspective of dynamical systems. Specifically, we establish the existence of a desirable equilibrium point for the GLOCAD and then prove that under some specific conditions, it is locally stable.

Note that the gradient descent update rule on (7) results in the following continuous dynamical system with the state space $\Phi = (\theta_g, \theta_d, \mathbb{V})$:

$$\begin{cases} \dot{\theta}_g := -\nabla_{\theta_g} \mathcal{L}(\theta_g, \theta_d, \mathbb{V}) \\ \dot{\theta}_d := \nabla_{\theta_d} \mathcal{L}(\theta_g, \theta_d, \mathbb{V}) \\ \dot{\mathbb{V}} := \nabla_{\mathbb{V}} \mathcal{L}(\theta_g, \theta_d, \mathbb{V}). \end{cases} \quad (8)$$

To investigate the stability of the GLOCAD, we consider the behaviour of the dynamical system (8) around its equilibrium state. Formally, the *equilibrium state* Φ^* is a desirable equilibrium if $P_{\mathbf{X}} = Q_{\mathbf{Y}} = G_{\theta_g^*}(\mathbf{Z})$, regardless of the values of θ_d and \mathbb{V} , and also the decoder $D_{\theta_d^*}$ is an injective function.

Proposition 1. *If the generator is realizable, i.e., there exists a $\theta_g^* \in \Theta_g$ such that $P_{\mathbf{X}} = Q_{\mathbf{Y}} = G_{\theta_g^*}(\mathbf{Z})$, the dynamical system of (8) has a desirable equilibrium $\Phi^* = (\theta_g^*, \theta_d, \mathbb{V})$ and this equilibrium is locally exponentially stable.*

To prove the existence, the objective function of each term is expanded and differentiated to obtain the dynamics of (8). It is then showed that, the rhs terms vanish at the equilibrium when $P_{\mathbf{X}} = Q_{\mathbf{Y}}$. To prove the local stability, we linearize the system around the desirable equilibrium point by computing the Jacobian of the dynamics. We then prove that the submatrix $\partial \dot{\theta}_g / \partial \theta_g$ of the Jacobian is *negative definite*, which is sufficient to conclude the stability of the system, e.g., see Nagarajan & Kolter 2017 and Wang et al. (2019, Lemma A.2). The detailed proof is given in Appendix A.

Proposition 1 implies that introducing trainable witness points in \mathbb{V} —in addition to the aforementioned benefits—do not harm our algorithm in terms of its stability.

4. Experiments

In this section, we present experimental results on simple simulations that treat the optimization problem as a dynamical system (Section 4.1 and 4.2) as well as on more realistic datasets, which give a better understanding of the interpretability of witness points (Section 4.3).

4.1. Simulation

First, we analyze the dynamics of GLOCAD on a one-dimensional problem with the analytic solution. The analysis aims to study the evolution of the parameters of the model under the dynamics of the gradient descent (GD). The GD is considered an update rule with infinitesimal step size resulting in a continuous dynamical system.

Single Gaussian. In this simulation, we assume that $P_{\mathbf{X}}$ is a one-dimensional Gaussian $\mathcal{N}(0, 1)$ and the model Q_{θ_q} is also Gaussian $\mathcal{N}(m_q, \sigma_q)$ parameterised by $\theta_q = \{m_q, \sigma_q\}$ where $\sigma_q = 1$. Moreover, the algorithm has access to only a

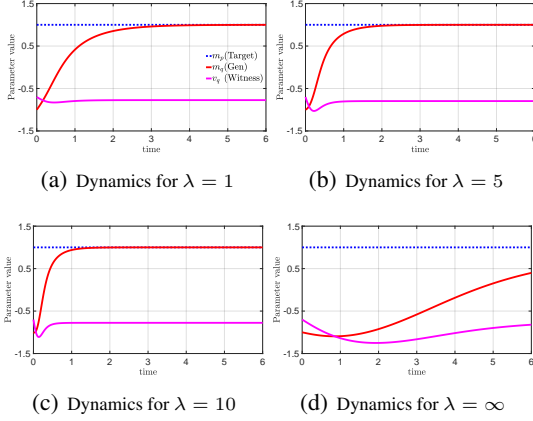


Figure 3. Numerical solution of the differential equations governing the GD learning of a mean of a Gaussian distribution. Color codes: (dashed blue) target value of the parameter, (red) learned value of the parameter (magenta) witness point. $\lambda = \infty$ means that only the UME term exists.

single witness point denoted by v . To analyze the dynamics of the GD, we first compute the loss function $\mathcal{L}(\theta_q, v)$ and then derive the governing dynamics for each of these parameters by calculating $d\theta_q/dt = -\nabla_{\theta_q}(\mathcal{L})$ and $dv/dt = \nabla_v(\mathcal{L})$.¹ Specifically, the loss function (7) becomes an MMD distance between two Gaussian distributions which is regularized by UME distance with λ as the regularization weight. Thus, the trainable parameters are m_q and v whose dynamics are governed by $\dot{v} = \nabla_v(\mu_P(v) - \mu_{\theta_q}(v))^2$ and $\dot{m}_q = -\nabla_{m_q}[\text{MMD}^2(m_q) + \lambda(\mu_P(v) - \mu_{\theta_q}(v))^2]$. This dynamical system is then solved numerically. Since we are interested in the role of UME, we study the effect of the governing dynamics on trajectories by changing the value of λ .

Fig. 3 depicts the results of this analysis. As we can see, the model parameter m_q converges to the target value and the witness point settles on a value different from the mean of the distributions. It is noteworthy that the final value of the witness point becomes irrelevant when the two distributions match, i.e., $(\mu_P(v) - \mu_{\theta_q}(v))^2 = 0$ for all v when $P = Q_{\theta_q}$. Moreover, we can also see in Fig. 3 that the speed of convergence is affected by the value of λ . The convergence gets slower for extremely low or large values of λ , suggesting that combining the two terms gives faster convergence than what could be achieved by either one alone.

Fig. 4 depicts the *phase portrait* of the dynamical system enforced by UME loss function in a region encompassing its equilibrium ($m_q = 0$) for different values of the kernel bandwidth. As can be seen, the system has a continuum of equilibria (depicted by the red line) rather than an iso-

¹See Appendix. B.1 for the details.

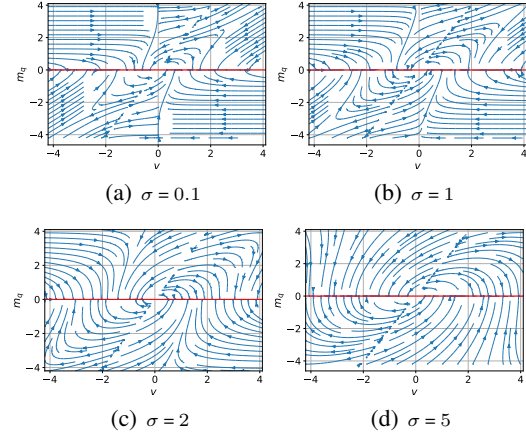


Figure 4. Phase portrait of the 2-dimensional dynamical system of Fig. 3 for various values of the kernel bandwidth σ . The plot manifests two equilibria : stable (The horizontal red line) and unstable (a line oriented in 45°).

lated equilibrium point. This phenomenon is proved for the general conditions briefly in Section 3.5 and in detail in Section A.1. This continuum is a stable equilibrium as it has an enclosing vicinity that every trajectory starting in this region converges to the equilibrium. This observation is also proved for the general case in Section 3.5 and Section A.2. It is noteworthy in Fig. 4 that the value of the kernel bandwidth changes the shape of the trajectories but leaves the locations of the equilibria unchanged.

Mixture of Gaussians. Next, we consider a multimodal target distribution $P_{\mathbf{X}} = 0.5 \cdot \mathcal{N}(1, 0.25) + 0.5 \cdot \mathcal{N}(-1, 0.25)$ and the model distribution $Q_{\theta_q} = 0.5 \cdot \mathcal{N}(m_1, 1) + 0.5 \cdot \mathcal{N}(m_2, 1)$ where $\theta_q = \{m_1, m_2\}$. We provide the algorithm with only one witness point v . Again, the loss function is MMD which is regularized by UME with λ as the regularization weight.² The differential equations are then solved numerically. Fig. 5 shows the trajectories of the parameters. Similar to the previous experiment, we observe that the fastest convergence occurs for a middle-valued λ that emphasizes the positive role of having UME along with the global term, which in this case is the MMD.

Spiky Gaussian. This experiment concerns the interpretation of GLOCAD as an adaptive filter as was put forward in Section 3.4. To elaborate more on this interpretation, we use a mixture of two Gaussians as the target distribution $P_{\mathbf{X}}$. Specifically, we consider $P_1 := \mathcal{N}(0, 1)$, $P_2 := \mathcal{N}(0, \sigma_q^2)$ where variance $\sigma_q^2 > 0$ and $P_{\mathbf{X}} := wP_1 + (1-w)P_2$ is defined on \mathbb{R} for some weight $w \in [0, 1]$. We are interested in the case where σ_q^2 is small, and w is close to 1. Consider a moment where the primary difference is local (at the origin),

²See Appendix. B.3 for the full derivation.

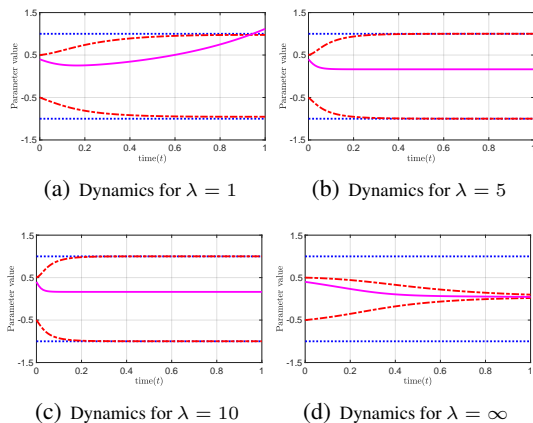


Figure 5. Numerical solution of the differential equations governing the GD learning of two means of a mixture of Gaussians when only one witness point is provided. The results are plotted for various values of the regularization weight λ . Color codes are the same as Fig. 3

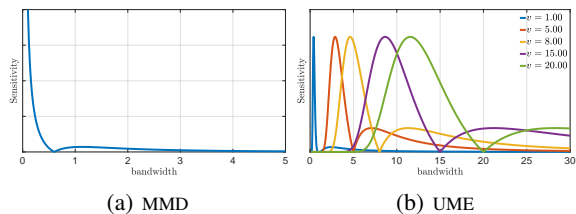


Figure 6. While MMD is indifferent to the presence of different frequencies in the target distribution (a), the UME can use its witness point to modulate its sensitivity to certain frequencies in the target distribution which are not yet captured by the model (b). $\lambda = \infty$ means that only the UME term exists

e.g., $Q = \mathcal{N}(0, 1)$. Because the second component (P_2) visually appears as a spike that rides on the wider Gaussian, we refer to P_X as a spiky Gaussian. Now we aim to approximate this distribution by a single Gaussian Q as the model. To show the sensitivity of MMD^2 and UME^2 in detecting the spiky component, we consider $\nabla_{\sigma_q} \text{MMD}^2$ and $\nabla_{\sigma_q} \text{UME}^2$. The two quantities are compared in Fig. 6. It can be seen in Fig. 6(a) that MMD has no freedom to change its sensitivity to different frequencies in the input. On the other hand, Fig. 6(b) shows that the sensitivity function of UME peaks at different locations by displacing witness points. This suggests that UME enjoys this extra degree of freedom provided by witness points to focus its attention on different bandwidths (frequencies) in the input which is similar to what adaptive filters carry out (Haykin, 2008).

4.2. Synthetic Dataset

In this section we increase the complexity of the problem by analyzing the performance of our method using a synthetic

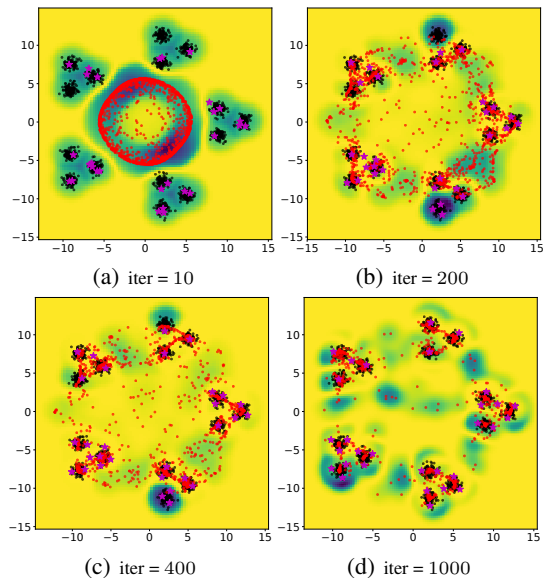


Figure 7. Two-dimensional mixture of Gaussian mixture models. Red dots: generated samples, black dots: target distribution, magenta stars: witness points, blue shade: the heatmap of the loss function of \mathbb{V} . The heatmap shows which areas of the space tend to absorb witness points during the optimization process.

two-dimensional dataset. We aim to investigate the role of witness points in capturing the local structure of P_X . We use a neural network to parameterize the generator as well as the witness points. The dataset used in this experiment is a mixture of Gaussian mixture models. The *outer* mixture places 5 components on a ring around the origin. Each of these components contains 3 Gaussian components which are also located on a smaller ring (see Fig. 7). The evolution of the generator (red dots) and witness points (magenta stars) in Fig. 7 shows that the global structure is initially captured by the generator; subsequently, the local structure of each component is captured by the witness points that act as guides for the generator to capture finer details of the distribution. Any missed mode is detected by the witness points which subsequently attract the probability mass of the generator. In absence of witness points, the global term (MMD) failed to capture all the modes unless the learning rate is set to about 100 times smaller which consequently makes the algorithm too slow to be used in practice. Moreover, not having the witness points, the global term does not inherently offer any possibility to probe the procedure in order to see which modes are not captured.

4.3. MNIST Dataset

To showcase the performance of Auto-GLOCAD and also the flexibility of the algorithm with respect to the first term of (7), we tested our method on a high-dimensional dataset, MNIST (LeCun et al., 1998) with Energy-Based

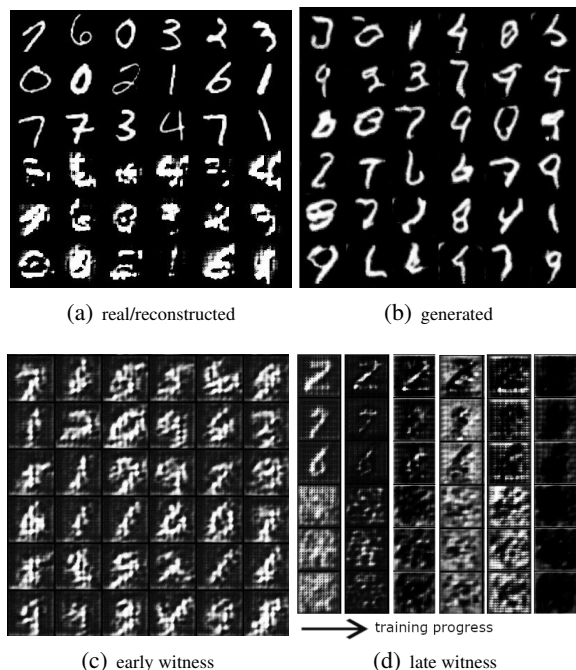


Figure 8. (a) Upper three rows show the real images ($x \in$ training set) and the lower three rows show their reconstructions by the autoencoder (b) Generated samples in a middle stage of the training process (c) The decoded learned witness points at early stages of Auto-GLOCAD (d) The progress of the witness points. Upper three rows are initialized to samples from the training set ($x \in \mathcal{X}$) and the lower three rows are initialized to ($G(z) \in \mathcal{Y}$). Initial states show the complete distinctions (almost clean images from $P_{\mathcal{X}}$ and unstructured noise from $Q_{\mathcal{Y}}$). In later stages of training, this clear distinction vanishes as the witness points become more and more similar.

GAN (Zhao et al., 2016). The discriminative function of this GAN is an autoencoder whose reconstruction loss is used to train the generator. According to Alg. 2, the witness points are defined and optimized in the latent space of this autoencoder. The results can be seen in Fig. 8. As depicted in Fig. 8(d), the progress of the witness points is informative about the training procedure. The algorithm is given 20 witness points, half of which initialized to $E_{\theta_a^e}(x)$ (for $x \in$ training set) and the other half initialized to $E_{\theta_a^e}(y)$ (for $y = G_{\theta_g}(z)$). The upper three rows of Fig. 8(d) show the progress of the first set and the lower three rows show the progress of the second set. In the beginning when $P_{\mathcal{X}}$ and $Q_{\mathcal{Y}}$ are completely distinct, the witness points converge to the support of the distributions (almost clear digits belonging to $P_{\mathcal{X}}$ in the upper rows and noisy images belonging to $Q_{\mathcal{Y}}$ in the lower rows). As the training proceeds, two sets of witness points become more and more similar implying that the distinctions between two distributions are getting smaller. Whenever a mismatch occurs between $P_{\mathcal{X}}$ and $Q_{\mathcal{Y}}$, a structured image appears in the witness points suggesting

that the distinction is more than noise. When the distributions match, we expect to see unstructured images in the witness points. See Appendix. E for another experiment on CIFAR-10 dataset (Liu et al., 2015).

5. Discussion and Conclusion

The stability problem of dynamical games that became popular in machine learning after the advent of GANs, has been approached by different strategies. One general stabilizing method is to introduce more players to the game with the hope that the introduction of the new states to the dynamical system gives a more stable algorithm. Neyshabur et al. proposed using multiple discriminators, each of which discriminates data distribution projected on a random axis. In practice, the number of projections should be large enough to ensure stability and random projections suffers from the lack of interpretability. Our work takes advantage of trainable witness points that make it possible to recover the distribution with much less projections. It is known that under mild assumptions, the population UME with any finite number of witness points defines an almost-sure metric on the space of probability measures (Chwialkowski et al., 2015, Theorem 2). Another work that roughly aligns with the line of our idea is (Denton et al., 2015) that trains multiple GANs for multiple resolutions of images created by Laplacian pyramid. The pyramid architecture and the resolutions are hard-coded and the algorithm has no freedom to design its own pyramid. The witness points of our work can be viewed as an adaptive pyramid with interpretability of the witness points as an added value. Among the works that combined autoencoder architecture with GANs, we found Sajjadi et al. (2018) roughly similar to our idea. They proposed to pass the data distribution through an autoencoder and use reconstructed data as the target distribution for a generator. However, since they still solve the problem in the data space rather than the latent space, the theoretical stability issues (Arjovsky & Bottou, 2017) remain unsolved (See Section. D for more detailed theoretical explanation).

To conclude, GLOCAD treats these problems by introducing witness points and optimizing them on a latent low-dimensional space of an autoencoder with equilibria whose stability is theoretically proved for Auto-GLOCAD. Moreover, the possibility to decode these witness points is another novelty of Auto-GLOCAD that makes it practically appealing. Our work shows the promising direction of algorithms with multiple components and multiple objectives. For the future, we can think of modular algorithms for which every module has a task such as: generative module (GAN), diagnosis module (witness points), and etc, that are trained together with different timescales. It is important to prove the stability of each module to make sure it does not harm the performance of the entire learning machine.

References

- Arbel, M., Sutherland, D., Binkowski, M., and Gretton, A. On gradient regularizers for mmd gans. *NeurIPS*, 2018.
- Arjovsky, M. and Bottou, L. Towards principled methods for training generative adversarial networks. In *International Conference on Learning Representations*, 2017.
- Arjovsky, M., Chintala, S., and Bottou, L. Wasserstein generative adversarial networks. In *ICML*, 2017.
- Arora, S., Risteski, A., and Zhang, Y. Do GANs learn the distribution? some theory and empirics. In *International Conference on Learning Representations*, 2018.
- Balduzzi, D., Racaniere, S., Martens, J., Foerster, J., Tuyls, K., and Graepel, T. The mechanics of n-player differentiable games. In *ICML*, 2018.
- Bińkowski, M., Sutherland, D., Arbel, M., and Gretton, A. Demystifying MMD GANs. *International Conference on Learning Representations*, 2018.
- Chen, X., Duan, Y., Houthoofd, R., Schulman, J., Sutskever, I., and Abbeel, P. Infogan: Interpretable representation learning by information maximizing generative adversarial nets. In *Advances in neural information processing systems*, pp. 2172–2180, 2016.
- Chwialkowski, K. P., Ramdas, A., Sejdinovic, D., and Gretton, A. Fast two-sample testing with analytic representations of probability measures. In *Advances in Neural Information Processing Systems 28*, pp. 1981–1989, 2015.
- Daskalakis, C., Ilyas, A., Syrgkanis, V., and Zeng, H. Training GANs with optimism. In *International Conference on Learning Representations*, 2018.
- Denton, E. L., Chintala, S., Fergus, R., et al. Deep generative image models using laplacian pyramid of adversarial networks. In *Advances in neural information processing systems*, pp. 1486–1494, 2015.
- Dziugaite, G. K., Roy, D. M., and Ghahramani, Z. Training generative neural networks via maximum mean discrepancy optimization. In *UAI*, 2015.
- Fukumizu, K., Gretton, A., Sun, X., and Schölkopf, B. Kernel measures of conditional dependence. In Platt, J. C., Koller, D., Singer, Y., and Roweis, S. T. (eds.), *Advances in Neural Information Processing Systems 20*, pp. 489–496. Curran Associates, Inc., 2008.
- Garreau, D., Jitkrittum, W., and Kanagawa, M. Large sample analysis of the median heuristic. *arXiv e-prints*, art. arXiv:1707.07269, July 2017.
- Goodfellow, I., Pouget-Abadie, J., Mirza, M., Xu, B., Warde-Farley, D., Ozair, S., Courville, A., and Bengio, Y. Generative adversarial networks. In *Advances in Neural Information Processing Systems*, pp. 2672–2680, 2014.
- Gretton, A., Borgwardt, K. M., Rasch, M. J., Schölkopf, B., and Smola, A. A kernel two-sample test. *Journal of Machine Learning Research*, 13(Mar):723–773, 2012. ISSN ISSN 1533-7928.
- Haykin, S. S. *Adaptive filter theory*. Pearson Education India, 2008.
- Hinton, G. E. and Salakhutdinov, R. R. Reducing the dimensionality of data with neural networks. *science*, 313 (5786):504–507, 2006.
- Jitkrittum, W., Szabó, Z., Chwialkowski, K. P., and Gretton, A. Interpretable distribution features with maximum testing power. In *Advances in Neural Information Processing Systems*, pp. 181–189, 2016.
- Karras, T., Aila, T., Laine, S., and Lehtinen, J. Progressive growing of GANs for improved quality, stability, and variation. In *International Conference on Learning Representations*, 2018.
- LeCun, Y., Bottou, L., Bengio, Y., and Haffner, P. Gradient-based learning applied to document recognition. *Proceedings of the IEEE*, 86(11):2278–2324, 1998.
- Li, C.-L., Chang, W.-C., Cheng, Y., Yang, Y., and Póczos, B. MMD GAN: Towards deeper understanding of moment matching network. In *Advances in Neural Information Processing Systems*, pp. 2203–2213, 2017a.
- Li, J., Monroe, W., Shi, T., Jean, S., Ritter, A., and Jurafsky, D. Adversarial learning for neural dialogue generation. In *Proceedings of the 2017 Conference on Empirical Methods in Natural Language Processing*, pp. 2157–2169. Association for Computational Linguistics, 2017b. doi: 10.18653/v1/D17-1230.
- Li, Y., Swersky, K., and Zemel, R. Generative moment matching networks. In *International Conference on Machine Learning*, pp. 1718–1727, 2015.
- Liu, Z., Luo, P., Wang, X., and Tang, X. Deep learning face attributes in the wild. In *Proceedings of International Conference on Computer Vision (ICCV)*, 2015.
- Loomis, L. H. *Introduction to abstract harmonic analysis*. Courier Corporation, 2013.
- Mehrjou, A. and Schölkopf, B. Nonstationary GANs: Analysis as nonautonomous dynamical systems. In *Workshop on Theoretical Foundations and Applications of Deep Generative Models at ICML*, July 2018.

- Mehrjou, A., Schölkopf, B., and Saremi, S. Annealed generative adversarial networks. *arXiv preprint arXiv:1705.07505*, 2017.
- Mehrjou, A., Khodabandeh, M., and Mori, G. Distribution aware active learning. *arXiv preprint arXiv:1805.08916*, 2018.
- Mescheder, L., Geiger, A., and Nowozin, S. Which training methods for GANs do actually converge? In *International Conference on Machine Learning*, pp. 3478–3487, 2018.
- Muandet, K., Fukumizu, K., Sriperumbudur, B., and Schölkopf, B. Kernel mean embedding of distributions: A review and beyond. *Foundations and Trends in Machine Learning*, 10(1-2):1–141, 2017.
- Müller, A. Integral probability metrics and their generating classes of functions. *Advances in Applied Probability*, 29(2):429–443, 1997.
- Nagarajan, V. and Kolter, J. Z. Gradient descent GAN optimization is locally stable. In *Advances in Neural Information Processing Systems*, pp. 5585–5595, 2017.
- Neyshabur, B., Bhojanapalli, S., and Chakrabarti, A. Stabilizing GAN Training with Multiple Random Projections. *ArXiv e-prints*, May 2017.
- Nowozin, S., Cseke, B., and Tomioka, R. f-GAN: Training generative neural samplers using variational divergence minimization. In *Advances in Neural Information Processing Systems*, pp. 271–279, 2016.
- Sajjadi, M. S., Parascandolo, G., Mehrjou, A., and Schölkopf, B. Tempered adversarial networks. In *ICLR Workshop*, 2018.
- Schropp, J. and Singer, I. A dynamical systems approach to constrained minimization. *Numerical functional analysis and optimization*, 21(3-4):537–551, 2000.
- Sertl, S. and Dellnitz, M. Global optimization using a dynamical systems approach. *Journal of Global Optimization*, 34(4):569–587, 2006.
- Smale, S. The prisoner’s dilemma and dynamical systems associated to non-cooperative games. *Econometrica: Journal of the Econometric Society*, pp. 1617–1634, 1980.
- Strang, G. *Introduction to linear algebra*, volume 3. Wellesley-Cambridge Press Wellesley, MA, 1993.
- Sutherland, D. J., Tung, H.-Y., Strathmann, H., De, S., Ramdas, A., Smola, A., and Gretton, A. Generative models and model criticism via optimized maximum mean discrepancy. In *International Conference on Learning Representations*, 2017.
- Wang, W., Sun, Y., and Halgamuge, S. Improving MMD-GAN training with repulsive loss function. In *International Conference on Learning Representations*, 2019.
- Wilson, A. C., Recht, B., and Jordan, M. I. A Lyapunov analysis of momentum methods in optimization. *arXiv preprint arXiv:1611.02635*, 2016.
- Zhao, J., Mathieu, M., and LeCun, Y. Energy-based generative adversarial network. *arXiv preprint arXiv:1609.03126*, 2016.
- Zhu, J.-Y., Park, T., Isola, P., and Efros, A. A. Unpaired image-to-image translation using cycle-consistent adversarial networks. In *Computer Vision (ICCV), 2017 IEEE International Conference on*, 2017.

Witnessing Adversarial Training in Reproducing Kernel Hilbert Spaces

Supplementary

A. Stability Analysis

In the following, we study the equilibria and the dynamical behaviour of the parameters of GLOCAD at the equilibrium. Our analysis is similar to that presented in Wang et al. (2019) and Nagarajan & Kolter (2017). Recall the following loss functions which are considered in GLOCAD:

$$L^{\text{mmd}} = \mathbb{E}_{P_{\mathbf{X}}}[k_D(\mathbf{x}, \mathbf{x}')] - 2\mathbb{E}_{P_{\mathbf{X}}, Q_{\mathbf{Y}}}[k_D(\mathbf{y}, \mathbf{y})] + \mathbb{E}_{Q_{\mathbf{Y}}}[k_D(\mathbf{y}, \mathbf{y}')] \quad (9a)$$

$$L^{\text{ume}} = \frac{1}{J} \sum_{j=1}^J (\mathbb{E}_{P_{\mathbf{X}}}[k_D(\mathbf{x}, \mathbf{v}_j)] - \mathbb{E}_{Q_{\mathbf{Y}}}[k_D(\mathbf{y}, \mathbf{v}_j)])^2 \quad (9b)$$

$$\mathcal{L} = L^{\text{mmd}} + \lambda L^{\text{ume}} \quad (9c)$$

where $k_D(\mathbf{x}, \mathbf{y}) = k(D(\mathbf{x}), D(\mathbf{y}))$ and $D : \mathcal{X} \rightarrow \mathcal{K}$ is the feature extractor which we will also call the discriminator interchangeably. Let $\theta_g \in \Theta_G$ and $\theta_d \in \Theta_D$ be the parameters of the discriminator and generator respectively. Let $\mathbb{V} = \{\mathbf{v}_j\}_{j=1}^J$ and $\mathbf{v}_j \in \mathcal{V}$ for $\mathcal{V} \subseteq \mathcal{K}$. The trainable parameters of GLOCAD are $\{\theta_g, \theta_d, \mathbb{V}\}$. Using gradient based optimization methods to find the optima of these losses gives us the following dynamical system when the learning rate of the optimization algorithm tends to zero ($\gamma \rightarrow 0$):

$$\begin{cases} \dot{\theta}_g = -\nabla_{\theta_g} \mathcal{L}(\theta_g, \theta_d, \mathbb{V}) \\ \dot{\theta}_d = \nabla_{\theta_d} \mathcal{L}(\theta_g, \theta_d, \mathbb{V}) \\ \dot{\mathbb{V}} = \nabla_{\mathbb{V}} \mathcal{L}(\theta_g, \theta_d, \mathbb{V}) \end{cases} \quad (10)$$

We proceed by making the following assumption about the equilibria of GLOCAD.

Assumption 1. At equilibrium $(\theta_g^*, \theta_d, \mathbb{V})$, we have $P_{\theta_g^*} = P_{\mathbf{X}}$ and $D_{\theta_d^*}(\mathbf{x})$ is injective on $\text{supp}(P_{\mathbf{X}}) \cup \text{supp}(P_{\theta_g^*})$.

The above assumption implies that at equilibrium the set of witness points $\mathbb{V} = \{\mathbf{v}_j\}_{j=1}^J$ can be arbitrary. That is, at equilibrium $L^{\text{ume}} = 0$ for any non-empty set \mathbb{V} . In what follows, we provide the detailed proof of Proposition 1.

A.1. Existence of Equilibria

Proposition A.1. If the generator is realizable, i.e., there exists a $\theta_g^* \in \Theta_G$ such that $Q_{\mathbf{Y}} = P_{\mathbf{X}}$, then the dynamical system of (10) has equilibria $(\theta_g^*, \theta_d, \mathbb{V})$ for any $\theta_d \in \Theta_D$ and $\mathbb{V} \in \mathcal{V}^J$.

Proof. Here, we expand the gradient of the loss (9) w.r.t. each set of trainable parameters to obtain the rhs of (10). Let $\mathbf{x} \sim P_{\mathbf{X}}$, $\mathbf{z} \sim P_{\mathbf{Z}}$, $\mathbf{Y} = G_{\theta_g}(\mathbf{Z}) \sim Q_{\mathbf{Y}}$. Suppose \mathbf{x} , \mathbf{z} and \mathbf{y} be realized samples from these distributions. Let denote the output of the $D(\cdot)$ by \mathbf{d} , i.e., $\mathbf{d}_x = D(\mathbf{x})$ and $\mathbf{d}_y = D(\mathbf{y})$. To ease the derivations, we assume that the kernel is isotropic stationary, i.e., $k(\mathbf{x}, \mathbf{y}) = \psi(\|\mathbf{x} - \mathbf{y}\|)$. The first term of (9c) is independent of \mathbb{V} and was proved to be stable in (Wang et al., 2019).

The second term L^{ume} is a function of all three set of trainable variables $\{\theta_g, \theta_d, \mathbb{V}\}$ and can be written as

$$\begin{aligned} L^{\text{ume}}(\theta_g, \theta_d, \mathbb{V}) &= \frac{1}{J} \sum_{j=1}^J \left(\mathbb{E}_{\mathbf{x} \sim P_{\mathbf{X}}} [k(D_{\theta_d}(\mathbf{x}), \mathbf{v}_j)] - \mathbb{E}_{\mathbf{y} \sim Q_{\mathbf{Y}}} [k(D_{\theta_d}(\mathbf{y}), \mathbf{v}_j)] \right)^2 \\ &= \frac{1}{J} \sum_{j=1}^J \left(\mathbb{E}_{\mathbf{x}}^2 [k(D_{\theta_d}(\mathbf{x}), \mathbf{v}_j)] - 2\mathbb{E}_{\mathbf{x}} [k(D_{\theta_d}(\mathbf{x}), \mathbf{v}_j)] \mathbb{E}_{\mathbf{y}} [k(D_{\theta_d}(\mathbf{y}), \mathbf{v}_j)] + \mathbb{E}_{\mathbf{y}}^2 [k(D_{\theta_d}(\mathbf{y}), \mathbf{v}_j)] \right), \end{aligned}$$

where $\mathbb{E}_{\mathbf{x}}[\cdot] := \mathbb{E}_{\mathbf{x} \sim P_{\mathbf{X}}}[\cdot]$ and $\mathbb{E}_{\mathbf{y}}[\cdot] := \mathbb{E}_{\mathbf{y} \sim Q_{\mathbf{Y}}}[\cdot]$. To simplify the notation, let $\mathbf{e}_{xv}^j = D(\mathbf{x}) - \mathbf{v}_j$ and $\mathbf{e}_{yv}^j = D(\mathbf{y}) - \mathbf{v}_j$, emphasizing our assumption that the kernel is isotropic. With slight abuse of notation, we simply use k instead of ψ

where $k(\mathbf{x}, \mathbf{y}) = \psi(\mathbf{x} - \mathbf{y})$. Because $\mathbf{y} = G_{\theta_g}(\mathbf{z})$, we rewrite $\mathbb{E}_{\mathbf{y}}[\cdot]$ as $\mathbb{E}_{\mathbf{z}}[\cdot]$. This re-parameterization is done since computing $\partial \mathbb{E}_{\mathbf{z}}[\cdot] / \partial \theta_g$ is much more convenient than $\partial \mathbb{E}_{\mathbf{y}}[\cdot] / \partial \theta_g$ due to the fact that the distribution with respect to which the expectation is taken is no longer a function of θ_g and we can swap the expectation with the derivation operators. Then, the dynamic of the system w.r.t. the parameters of the generator can be written as

$$\dot{\theta}_g = -\frac{1}{J} \sum_{j=1}^J \left(2\mathbb{E}_{\mathbf{x}}[k_D(\mathbf{x}, \mathbf{v}_j)] \mathbb{E}_{\mathbf{x}} \left[\frac{\partial k_D}{\partial \mathbf{e}_{\mathbf{x}\mathbf{v}}^j} \frac{\partial \mathbf{e}_{\mathbf{x}\mathbf{v}}^j}{\partial \theta_g} \right] - 2\mathbb{E}_{\mathbf{x}}[k_D(\mathbf{x}, \mathbf{v}_j)] \mathbb{E}_{\mathbf{z}} \left[\frac{\partial k_D}{\partial \mathbf{e}_{\mathbf{y}\mathbf{v}}^j} \frac{\partial \mathbf{e}_{\mathbf{y}\mathbf{v}}^j}{\partial \theta_g} \right] \right. \\ \left. - 2\mathbb{E}_{\mathbf{z}}[k_D(\mathbf{y}, \mathbf{v}_j)] \mathbb{E}_{\mathbf{x}} \left[\frac{\partial k_D}{\partial \mathbf{e}_{\mathbf{x}\mathbf{v}}^j} \frac{\partial \mathbf{e}_{\mathbf{x}\mathbf{v}}^j}{\partial \theta_g} \right] + 2\mathbb{E}_{\mathbf{z}}[k_D(\mathbf{y}, \mathbf{v}_j)] \mathbb{E}_{\mathbf{z}} \left[\frac{\partial k_D}{\partial \mathbf{e}_{\mathbf{y}\mathbf{v}}^j} \frac{\partial \mathbf{e}_{\mathbf{y}\mathbf{v}}^j}{\partial \theta_g} \right] \right) \quad (11)$$

$$= -\frac{1}{J} \sum_{j=1}^J \left(2(\mathbb{E}_{\mathbf{z}}[k_D(\mathbf{y}, \mathbf{v}_j)] - \mathbb{E}_{\mathbf{x}}[k_D(\mathbf{x}, \mathbf{v}_j)]) \mathbb{E}_{\mathbf{z}} \left[\frac{\partial k_D}{\partial \mathbf{e}_{\mathbf{y}\mathbf{v}}^j} \frac{\partial \mathbf{e}_{\mathbf{y}\mathbf{v}}^j}{\partial \theta_g} \right] \right) \quad (12)$$

$$= 0, \quad (13)$$

where we used the fact that $\frac{\partial \mathbf{e}_{\mathbf{x}\mathbf{v}}^j}{\partial \theta_g} = 0$ to derive (12). The last equality (12) follows from the fact that $\mathbb{E}_{\mathbf{z}}[k_D(\mathbf{y}, \mathbf{v}_j)] - \mathbb{E}_{\mathbf{x}}[k_D(\mathbf{x}, \mathbf{v}_j)]$ vanishes at the equilibrium (when $P_{\mathbf{X}} = Q_{\mathbf{Y}}$), see Assumption 1.

Similarly, the dynamics of the parameters of the feature extractor θ_d can be written as

$$\dot{\theta}_d = \frac{1}{J} \sum_{j=1}^J \left(2\mathbb{E}_{\mathbf{x}}[k_D(\mathbf{x}, \mathbf{v}_j)] \mathbb{E}_{\mathbf{x}} \left[\frac{\partial k_D}{\partial \mathbf{e}_{\mathbf{x}\mathbf{v}}^j} \frac{\partial \mathbf{e}_{\mathbf{x}\mathbf{v}}^j}{\partial \theta_d} \right] - 2\mathbb{E}_{\mathbf{x}}[k_D(\mathbf{x}, \mathbf{v}_j)] \mathbb{E}_{\mathbf{z}} \left[\frac{\partial k_D}{\partial \mathbf{e}_{\mathbf{y}\mathbf{v}}^j} \frac{\partial \mathbf{e}_{\mathbf{y}\mathbf{v}}^j}{\partial \theta_d} \right] \right. \\ \left. - 2\mathbb{E}_{\mathbf{z}}[k_D(\mathbf{y}, \mathbf{v}_j)] \mathbb{E}_{\mathbf{x}} \left[\frac{\partial k_D}{\partial \mathbf{e}_{\mathbf{x}\mathbf{v}}^j} \frac{\partial \mathbf{e}_{\mathbf{x}\mathbf{v}}^j}{\partial \theta_d} \right] + 2\mathbb{E}_{\mathbf{z}}[k_D(\mathbf{y}, \mathbf{v}_j)] \mathbb{E}_{\mathbf{z}} \left[\frac{\partial k_D}{\partial \mathbf{e}_{\mathbf{y}\mathbf{v}}^j} \frac{\partial \mathbf{e}_{\mathbf{y}\mathbf{v}}^j}{\partial \theta_d} \right] \right) \\ = \frac{1}{J} \sum_{j=1}^J \left(2(\mathbb{E}_{\mathbf{x}}[k_D(\mathbf{x}, \mathbf{v}_j)] - \mathbb{E}_{\mathbf{z}}[k_D(\mathbf{y}, \mathbf{v}_j)]) \mathbb{E}_{\mathbf{x}} \left[\frac{\partial k_D}{\partial \mathbf{e}_{\mathbf{x}\mathbf{v}}^j} \frac{\partial \mathbf{e}_{\mathbf{x}\mathbf{v}}^j}{\partial \theta_d} \right] \right. \\ \left. + 2(\mathbb{E}_{\mathbf{z}}[k_D(\mathbf{y}, \mathbf{v}_j)] - \mathbb{E}_{\mathbf{x}}[k_D(\mathbf{x}, \mathbf{v}_j)]) \mathbb{E}_{\mathbf{x}} \left[\frac{\partial k_D}{\partial \mathbf{e}_{\mathbf{y}\mathbf{v}}^j} \frac{\partial \mathbf{e}_{\mathbf{y}\mathbf{v}}^j}{\partial \theta_d} \right] \right) \\ = 0, \quad (14)$$

where we used the fact that $\mathbb{E}_{\mathbf{z}}[k_D(\mathbf{y}, \mathbf{v}_j)] - \mathbb{E}_{\mathbf{x}}[k_D(\mathbf{x}, \mathbf{v}_j)]$ vanishes at the equilibrium.

Finally, the dynamics of the witness points can be written as

$$\dot{\mathbf{v}}_j = \frac{1}{J} \sum_{j=1}^J \left(2\mathbb{E}_{\mathbf{x}}[k_D(\mathbf{x}, \mathbf{v}_j)] \mathbb{E}_{\mathbf{x}} \left[\frac{\partial k_D}{\partial \mathbf{e}_{\mathbf{x}\mathbf{v}}^j} \frac{\partial \mathbf{v}_j}{\partial \mathbf{v}_j} \right] - 2\mathbb{E}_{\mathbf{x}}[k_D(\mathbf{x}, \mathbf{v}_j)] \mathbb{E}_{\mathbf{z}} \left[\frac{\partial k_D}{\partial \mathbf{e}_{\mathbf{y}\mathbf{v}}^j} \frac{\partial \mathbf{v}_j}{\partial \mathbf{v}_j} \right] \right. \\ \left. - 2\mathbb{E}_{\mathbf{z}}[k_D(\mathbf{y}, \mathbf{v}_j)] \mathbb{E}_{\mathbf{x}} \left[\frac{\partial k_D}{\partial \mathbf{e}_{\mathbf{x}\mathbf{v}}^j} \frac{\partial \mathbf{v}_j}{\partial \mathbf{v}_j} \right] + 2\mathbb{E}_{\mathbf{z}}[k_D(\mathbf{y}, \mathbf{v}_j)] \mathbb{E}_{\mathbf{z}} \left[\frac{\partial k_D}{\partial \mathbf{e}_{\mathbf{y}\mathbf{v}}^j} \frac{\partial \mathbf{v}_j}{\partial \mathbf{v}_j} \right] \right) \quad (15)$$

$$= \frac{1}{J} \sum_{j=1}^J \left(2(\mathbb{E}_{\mathbf{x}}[k_D(\mathbf{x}, \mathbf{v}_j)] - \mathbb{E}_{\mathbf{z}}[k_D(\mathbf{y}, \mathbf{v}_j)]) \mathbb{E}_{\mathbf{x}} \left[\frac{\partial k_D}{\partial \mathbf{e}_{\mathbf{x}\mathbf{v}}^j} \frac{\partial \mathbf{v}_j}{\partial \mathbf{v}_j} \right] \right) \quad (16)$$

$$+ 2(\mathbb{E}_{\mathbf{z}}[k_D(\mathbf{y}, \mathbf{v}_j)] - \mathbb{E}_{\mathbf{x}}[k_D(\mathbf{x}, \mathbf{v}_j)]) \mathbb{E}_{\mathbf{x}} \left[\frac{\partial k_D}{\partial \mathbf{e}_{\mathbf{y}\mathbf{v}}^j} \frac{\partial \mathbf{v}_j}{\partial \mathbf{v}_j} \right] \quad (17)$$

$$= 0, \quad (18)$$

where we used the same argument as above to conclude that $\dot{\mathbf{v}}_j$ vanishes at the equilibrium.

Above analysis show that $(\dot{\theta}_g, \dot{\theta}_d, \dot{\mathbf{v}})$ vanishes at an equilibrium where $P_{\mathbf{X}} = Q_{\mathbf{Y}=G_{\theta_g^*}(\mathbf{z})}$. Notice that the equilibrium is not an isolated point in the space of parameters. In fact, $\mathcal{E} = \{(\theta_g^*, \theta_d, \mathbf{v}) \text{ for all } \theta_d \in \Theta_D\}$ is the set of equilibria that is an

equilibrium subspace $\mathcal{E} \subset \Theta_G \times \Theta_D \times \mathcal{V}^J$ instead of an isolated equilibrium point. In other words, we have continuum of equilibria rather than isolated equilibria. \square

A.2. Local Stability

Given that a desirable equilibrium exists as shown in Proposition A.1, we are now in a position to show the local stability of this equilibrium subspace.

Lemma A.1 (Nagarajan & Kolter 2017; Wang et al. 2019). *Consider a non-linear system of parameters (θ, γ) : $\dot{\theta} = h_1(\theta, \gamma)$, $\dot{\gamma} = h_2(\theta, \gamma)$ with an equilibrium point at $(\mathbf{0}, \mathbf{0})$. Let there exist ϵ such that $\forall \gamma \in \mathbb{B}_\epsilon(\mathbf{0})$, $(\mathbf{0}, \gamma)$ is an equilibrium. If $\mathbf{J} = \left. \frac{\partial h_1(\theta, \gamma)}{\partial \theta} \right|_{(\mathbf{0}, \mathbf{0})}$ is a Hurwitz matrix, the non-linear system is exponentially stable.*

Proposition A.2. *The non-linear dynamical system with states $\Phi = (\theta_g, \theta_d, \mathbb{V})$ is exponentially stable at its equilibrium $(\theta_g^*, \theta_d, \mathbb{V})$ for any $\theta_d \in \Theta_d$ and $\mathbb{V} \in \mathcal{V}^J$.*

Proof. We start off with deriving the Jacobian of the system (10) as

$$\mathbf{J} \triangleq \begin{bmatrix} \partial \dot{\theta}_g^T / \partial \theta_g & \partial \dot{\theta}_g^T / \partial \theta_d & \partial \dot{\theta}_g^T / \partial \mathbb{V} \\ \partial \dot{\theta}_d^T / \partial \theta_g & \partial \dot{\theta}_d^T / \partial \theta_d & \partial \dot{\theta}_d^T / \partial \mathbb{V} \\ \partial \dot{\mathbb{V}}^T / \partial \theta_g & \partial \dot{\mathbb{V}}^T / \partial \theta_d & \partial \dot{\mathbb{V}}^T / \partial \mathbb{V} \end{bmatrix}. \quad (19)$$

For simplicity, we assume that the effect of the feature extractor is absorbed in the kernel and $k_D(\mathbf{x}, \mathbf{y}) = k(D(\mathbf{x}), D(\mathbf{y})) = k(\mathbf{x}, \mathbf{y}) = k_{\mathbf{x}\mathbf{y}}$ and the kernel is radial $k(\mathbf{x}, \mathbf{y}) = k(\|\mathbf{x} - \mathbf{y}\|) = k(\mathbf{x}\mathbf{y})$ where $\mathbf{x}\mathbf{y}$ is a scalar. Notice that $\mathbf{x}\mathbf{y}$ is not a multiplication. It only denotes a scalar which is a function of both \mathbf{x} and \mathbf{y} . This simplifies the derivatives to a great extent. To further simplify the notations of partial derivatives, let $\Delta_b^a = \frac{\partial^2 a}{\partial b^2}$ and $\Delta_{bc}^a = \frac{\partial^2 a}{\partial b \partial c}$. In addition, we only consider a single witness point (v), i.e., $J = 1$. The loss function is then simplified as

$$\mathcal{L}^{\text{ume}} = \mathbb{E}_x^2[k(\mathbf{x}v)] + \mathbb{E}_z^2[k(\mathbf{y}v)] - 2\mathbb{E}_x[k(\mathbf{x}v)]\mathbb{E}_z[k(\mathbf{y}v)]. \quad (20)$$

Assume the only trainable parameters are the parameters of the generator $\theta = \theta_g$ and the witness point v . The dynamical system is then simplified as

$$\dot{\theta} = -2\mathbb{E}_z[k(\mathbf{y}v)]\mathbb{E}_z[k'_{\mathbf{y}v}\nabla_{\theta}^{\mathbf{y}v}] + 2\mathbb{E}_x[k(\mathbf{x}v)]\mathbb{E}_z[k'_{\mathbf{y}v}\nabla_{\theta}^{\mathbf{y}v}] \quad (21)$$

$$\dot{v} = 2\mathbb{E}_x[k(\mathbf{x}v)]\mathbb{E}_x[k'_{\mathbf{x}v}\nabla_v^{\mathbf{x}v}] + 2\mathbb{E}_z[k(\mathbf{y}v)]\mathbb{E}_z[k'_{\mathbf{y}v}\nabla_v^{\mathbf{y}v}] - 2\mathbb{E}_x[k(\mathbf{x}v)]\mathbb{E}_z[k'_{\mathbf{y}v}\nabla_v^{\mathbf{y}v}]. \quad (22)$$

The Jacobian matrix

$$\mathbf{J} \triangleq \begin{bmatrix} \mathbf{J}_{GG} & \mathbf{J}_{GV} \\ \mathbf{J}_{VG} & \mathbf{J}_{VV} \end{bmatrix} = \begin{bmatrix} \partial \dot{\theta}^T / \partial \theta & \partial \dot{\theta}^T / \partial v \\ \partial \dot{v}^T / \partial \theta & \partial \dot{v}^T / \partial v \end{bmatrix} \quad (23)$$

then describes the behaviour of the system around the equilibrium point. Moreover, we have

$$\frac{1}{2}\mathbf{J}_{GG} = -\mathbb{E}_z[k'_{\mathbf{y}v}{}^2\Delta_{\theta}^{\mathbf{y}v}]\mathbb{E}_z[k'_{\mathbf{y}v}{}^2\Delta_{\theta}^{\mathbf{y}v\top}] + \mathbb{E}_z[k(\mathbf{y}v)]\mathbb{E}_z[k''_{\mathbf{y}v}\Delta_{\theta}^{\mathbf{y}v} + k'_{\mathbf{y}v}\Delta_{\theta}^{\mathbf{y}v}] \quad (24)$$

$$= -\mathbb{E}_x[k(\mathbf{x}v)]\mathbb{E}_z[k'_{\mathbf{y}v}\Delta_{\theta}^{\mathbf{y}v} + k'_{\mathbf{y}v}\Delta_{\theta}^{\mathbf{y}v}] \\ = -\mathbb{E}_z[k'_{\mathbf{y}v}{}^2\Delta_{\theta}^{\mathbf{y}v}]\mathbb{E}_z[k'_{\mathbf{y}v}{}^2\Delta_{\theta}^{\mathbf{y}v\top}] + (\mathbb{E}_z[k(\mathbf{y}v)] - \mathbb{E}_x[k(\mathbf{x}v)])\mathbb{E}_z[k''_{\mathbf{y}v}\Delta_{\theta}^{\mathbf{y}v} + k'_{\mathbf{y}v}\Delta_{\theta}^{\mathbf{y}v}] \quad (25)$$

$$= -\mathbb{E}_z[k'_{\mathbf{y}v}{}^2\Delta_{\theta}^{\mathbf{y}v}]\mathbb{E}_z[k'_{\mathbf{y}v}{}^2\Delta_{\theta}^{\mathbf{y}v\top}] \leq 0. \quad (26)$$

Since $(\mathbb{E}_z[k(\mathbf{y}v)] - \mathbb{E}_x[k(\mathbf{x}v)]) = 0$ at the equilibrium when $P_X = Q_Y$ (See Assumption 1), the second term of (25) vanishes at the equilibrium. The last line follows from the fact that $\mathbf{M}\mathbf{M}^T$ is positive semidefinite for every matrix $\mathbf{M} \in \mathbb{R}^{m \times n}$ (Strang, 1993). Having proved that \mathbf{J}_{GG} is negative definite makes it straightforward, inspired by Nagarajan & Kolter (2017)(Lemma C.3), to take the last step and show the local exponential stability of the system. The sketch of the proof is to expand the eigenvalue decomposition of \mathbf{J}_{GG} and projecting the system to the subspace that is orthogonal to the equilibria. The resultant projected system has a Hurwitz Jacobian matrix ensuring the exponential stability of the system in the subspace orthogonal to the equilibria. The result then follows from Lemma A.1 (See the last step of the proof of the Proposition 1 of (Wang et al., 2019)). \square

B. Derivation of the Analytical Dynamics Function

Here we derive the formulation of the dynamical system of (8) for simple tractable cases which are used to simulate the dynamical systems of section 4.1. We first reproduce a well-known lemma that will be useful for derivations to come.

Lemma B.1 (Gaussian integral computation (Garreau et al. (2017), Lemma E.1)). *Let $a, b, c, d \in \mathbb{R}$ with $b, d > 0$. Then*

$$\frac{1}{\sqrt{2\pi}} \int \exp\left(\frac{-(x-a)^2}{b} + \frac{-(x-c)^2}{d}\right) dx = \sqrt{\frac{bd}{2(b+d)}} \exp\left(\frac{-(a-c)^2}{b+d}\right).$$

B.1. Single Gaussian

Assume $P = \mathcal{N}(m_p, \sigma_p^2)$, $Q = \mathcal{N}(m_q, \sigma_q^2)$ and $k(x, y) = \exp\left(-\frac{(x-y)^2}{2\sigma^2}\right)$ be a Gaussian kernel with bandwidth σ^2 .

$$\begin{aligned} \mu_P(v) &= \int k(x, v)p(x)dx \\ &= \frac{1}{\sigma_p} \frac{1}{\sqrt{2\pi}} \int \exp\left(-\frac{(x-v)^2}{2\sigma^2} - \frac{(x-m_p)^2}{2\sigma_p^2}\right) dx \\ &\stackrel{(a)}{=} \sqrt{\frac{\sigma^2}{\sigma^2 + \sigma_p^2}} \exp\left(-\frac{(v-m_p)^2}{2(\sigma^2 + \sigma_p^2)}\right), \end{aligned} \tag{27}$$

where at (a) we use Lemma B.1. It follows that

$$\begin{aligned} &(\mu_P(v) - \mu_\theta(v))^2 \\ &= \mu_P^2(v) + \mu_Q^2(v) - 2\mu_P(v)\mu_Q(v) \\ &= \frac{\sigma^2}{\sigma^2 + \sigma_p^2} \exp\left(-\frac{(v-m_p)^2}{\sigma^2 + \sigma_p^2}\right) + \frac{\sigma^2}{\sigma^2 + \sigma_q^2} \exp\left(-\frac{(v-m_q)^2}{\sigma^2 + \sigma_q^2}\right) \\ &\quad - 2\sqrt{\frac{\sigma^2}{\sigma^2 + \sigma_p^2} \frac{\sigma^2}{\sigma^2 + \sigma_q^2}} \exp\left(-\frac{(v-m_p)^2}{2(\sigma^2 + \sigma_p^2)} - \frac{(v-m_q)^2}{2(\sigma^2 + \sigma_q^2)}\right). \end{aligned}$$

After further simplification $p = \mathcal{N}(0, 1)$, $q = \mathcal{N}(m_q, 1)$ and $\theta = m_q$, we have

$$\begin{aligned} (\mu_P(v) - \mu_\theta(v))^2 &= \frac{\sigma^2}{\sigma^2 + 1} \exp\left(-\frac{v^2}{\sigma^2 + 1}\right) + \frac{\sigma^2}{\sigma^2 + 1} \exp\left(-\frac{(v-m_q)^2}{\sigma^2 + 1}\right) \\ &\quad - 2\frac{\sigma^2}{\sigma^2 + 1} \exp\left(-\frac{v^2}{2(\sigma^2 + 1)} - \frac{(v-m_q)^2}{2(\sigma^2 + 1)}\right). \end{aligned}$$

giving rise to the following gradient vector field

$$\begin{aligned} \frac{dv}{dt} &= \nabla_v(\mu_P(v) - \mu_\theta(v))^2 = -\frac{2\sigma^2}{(\sigma^2 + 1)^2} v \exp\left(-\frac{v^2}{\sigma^2 + 1}\right) - \frac{2\sigma^2}{(\sigma^2 + 1)^2} (v - m_q) \exp\left(-\frac{(v-m_q)^2}{\sigma^2 + 1}\right) \\ &\quad + \frac{2\sigma^2}{(\sigma^2 + 1)^2} (2v - m_q) \exp\left(-\frac{v^2 + (v-m_q)^2}{2(\sigma^2 + 1)}\right). \end{aligned}$$

Similarly, we have

$$\begin{aligned} \frac{dm_q}{dt} &= -\nabla_{m_q}(\mu_P(v) - \mu_\theta(v))^2 = -\frac{2\sigma^2}{(\sigma^2 + 1)^2} (v - m_q) \exp\left(-\frac{(v-m_q)^2}{\sigma^2 + 1}\right) \\ &\quad + \frac{2\sigma^2}{(\sigma^2 + 1)^2} (v - m_q) \exp\left(-\frac{v^2 + (v-m_q)^2}{2(\sigma^2 + 1)}\right) \\ &= -\frac{2\sigma^2}{(\sigma^2 + 1)^2} (v - m_q) \left[\exp\left(-\frac{(v-m_q)^2}{\sigma^2 + 1}\right) - \exp\left(-\frac{v^2 + (v-m_q)^2}{2(\sigma^2 + 1)}\right) \right]. \end{aligned}$$

B.2. Spiky Gaussian

Let $P_1 := \mathcal{N}(0, 1)$, $P_2 := \mathcal{N}(0, \sigma_q^2)$ and $P := wP_1 + (1 - w)P_2$ defined on \mathbb{R} for some weight $w \in [0, 1]$ and variance σ_q^2 . When σ_q^2 is small, the two distributions illustrate a case where the primary difference is local (at the origin). Consider a moment when the trainable distribution (model) is $Q = \mathcal{N}(0, 1)$. We refer to P as a spiky Gaussian. Assume a Gaussian kernel $k(x, y) = \exp\left(-\frac{(x-y)^2}{2\sigma^2}\right)$ for some bandwidth $\sigma^2 > 0$.

MMD We have

$$\begin{aligned} \text{MMD}^2(P, Q) &= \mathbb{E}_{x, x' \sim P} k(x, x') + \mathbb{E}_{y, y' \sim Q} k(y, y') - 2\mathbb{E}_{x \sim P} \mathbb{E}_{y \sim Q} k(x, y) \\ &\stackrel{(a)}{=} (1 - w)^2 [c(2) + c(2\sigma_q^2) - 2c(1 + \sigma_q^2)], \end{aligned}$$

where we note that all the expectations in the first line are Gaussian integrals and use Lemma B.1 to simplify all the expressions at (a), and $c(z) := \sqrt{\frac{\sigma^2}{\sigma^2 + z}}$ for $z > 0$. Note that when $w = 1$ or $\sigma_q^2 = 1$, $P = Q$ and $\text{MMD}^2(P, Q) = 0$.

UME With the help of Lemma B.1, we have similarly

$$\begin{aligned} \mu_Q(v) &= \mathbb{E}_{y \sim Q} k(y, v) = c(1) \exp\left(\frac{-v^2}{2(\sigma^2 + 1)}\right), \\ \mu_P(v) &= w\mathbb{E}_{x \sim Q} k(x, v) + (1 - w)\mathbb{E}_{x \sim P_2} k(x, v) \\ &= w\mu_Q(v) + (1 - w)c(\sigma_q^2) \exp\left(\frac{-v^2}{2(\sigma^2 + \sigma_q^2)}\right). \end{aligned}$$

It follows that

$$\begin{aligned} \text{UME}^2(P, Q) &= (\mu_P(v) - \mu_Q(v))^2 \\ &= (1 - w)^2 \left[c(1) \exp\left(\frac{-v^2}{2(\sigma^2 + 1)}\right) - c(\sigma_q^2) \exp\left(\frac{-v^2}{2(\sigma^2 + \sigma_q^2)}\right) \right]^2. \end{aligned}$$

The derivatives of these loss functions with respect to s_q are taken for the sensitivity analysis.

$$\frac{\partial(\text{MMD}^2)}{\partial s_q} = \frac{s_q s^2}{2\sqrt{\frac{s^2}{s^2 + s_q^2} + 1} (s^2 + s_q^2 + 1)^2} - \frac{s^2}{4(s^2 + 2s_q)^2 \sqrt{\frac{s^2}{s^2 + 2s_q}}} \quad (28)$$

$$\begin{aligned} \frac{\partial(\text{UME}^2)}{\partial s_q} &= -2 \left(\frac{\exp\left(-\frac{v^2}{2s^2 + 2}\right) \sqrt{\frac{s^2}{s^2 + 1}}}{2} - \frac{\exp\left(-\frac{v^2}{2s^2 + 2s_q^2}\right) \exp\left(\frac{s^2}{s^2 + s_q^2}\right)}{2} \right) \\ &\quad \left(\frac{2s_q v^2 \exp\left(-\frac{v^2}{2s^2 + 2s_q^2}\right) \sqrt{\frac{s^2}{s^2 + s_q^2}}}{(2s^2 + 2s_q^2)^2} - \frac{s^2 s_q \exp\left(-\frac{v^2}{2s^2 + 2s_q^2}\right)}{2(s^2 + s_q^2)^2 \sqrt{\frac{s^2}{s^2 + s_q^2}}} \right). \end{aligned} \quad (29)$$

B.3. Mixture of Gaussians

Assume that $p(x) := \sum_{j=1}^{c_p} \omega_{p,j} \mathcal{N}(x | m_{p,j}, \sigma_{p,j}^2) := \sum_{j=1}^{c_p} \omega_{p,j} p_j(x)$ where we define the j^{th} component $p_j(x) := \mathcal{N}(x | m_{p,j}, \sigma_{p,j}^2)$, $\boldsymbol{\omega}_p := (\omega_{p,1}, \dots, \omega_{p,c_p})^\top$ is a vector of non-negative mixing weights such that $\sum_{j=1}^{c_p} \omega_{p,j} = 1$, $\{m_{p,j}\}_{j=1}^{c_p}$ are the means of the $c_p > 0$ components, and $\{\sigma_{p,j}^2\}_{j=1}^{c_p}$ are the variances. Similarly, assume that $q(y) := \sum_{j=1}^{c_q} \omega_{q,j} \mathcal{N}(y | m_{q,j}, \sigma_{q,j}^2)$. It follows from (27) that the mean embedding μ_p of p w.r.t a Gaussian kernel with bandwidth σ^2 is

$$\begin{aligned} \mu_p(v) &= \sum_{j=1}^{c_p} \omega_{p,j} \mu_{p_j}(v) \\ &= \sum_{j=1}^{c_p} \omega_{p,j} \sqrt{\frac{\sigma^2}{\sigma^2 + \sigma_{p,j}^2}} \exp\left(-\frac{(v - m_{p,j})^2}{2(\sigma^2 + \sigma_{p,j}^2)}\right). \end{aligned}$$

C. Interpretation as Change of Coordinates

Let $\mu_P := \mathbb{E}_{\mathbf{x} \sim P}[\phi(\mathbf{x})]$ be the mean embedding of P in a Hilbert space \mathcal{H} . The UME between P and Q is defined as

$$\begin{aligned} \text{UME}^2(P_{\mathbf{X}}, Q_{\mathbf{Y}}) &:= \frac{1}{J} \sum_{j=1}^J (\mu_P(\mathbf{v}_j) - \mu_Q(\mathbf{v}_j))^2 \\ &= \left\langle (\mu_P - \mu_Q), \left(\frac{1}{J} \sum_{j=1}^J \phi(\mathbf{v}_j) \otimes \phi(\mathbf{v}_j) \right) (\mu_P - \mu_Q) \right\rangle_{\mathcal{H}}, \end{aligned}$$

where \otimes denotes the outer product, and $\langle \cdot, \cdot \rangle_{\mathcal{H}}$ denotes the inner product on \mathcal{H} . Our regularized objective is

$$\begin{aligned} \text{MMD}^2(P, Q) + \lambda \text{UME}^2(P, Q) &= \|\mu_P - \mu_Q\|^2 + \lambda \frac{1}{J} \sum_{j=1}^J (\mu_P(\mathbf{v}_j) - \mu_Q(\mathbf{v}_j))^2 \\ &= \left\langle (\mu_P - \mu_Q), \left(I + \frac{\lambda}{J} \sum_{j=1}^J \phi(\mathbf{v}_j) \otimes \phi(\mathbf{v}_j) \right) (\mu_P - \mu_Q) \right\rangle_{\mathcal{H}}, \end{aligned}$$

where $I: \mathcal{H} \rightarrow \mathcal{H}$ is the identity operator.

Consider $\phi(\mathbf{x}) = \mathbf{x}$ i.e., a linear kernel. Then the regularized objective becomes

$$(\mu_P - \mu_Q)^\top \left(I + \frac{\lambda}{J} \sum_{j=1}^J \mathbf{v}_j \mathbf{v}_j^\top \right) (\mu_P - \mu_Q),$$

where μ_P is simply the first moment of P .

If we assume orthonormal witness points $\{\mathbf{v}_j\}_{j=1}^J$, we can then view $A = \sum_{j=1}^J \mathbf{v}_j \mathbf{v}_j^\top$ as the eigenvalue decomposition of A . This basically means that the term $\frac{\lambda}{J} \sum_{j=1}^J \mathbf{v}_j \mathbf{v}_j^\top$ performs a change of coordinates by a rotation matrix whose eigen vectors are \mathbf{v}_j . During the optimization of the following loss function

$$\mathcal{L} = (\mu_P - \mu_Q)^\top \left(I + \frac{\lambda}{J} \sum_{j=1}^J \mathbf{v}_j \mathbf{v}_j^\top \right) (\mu_P - \mu_Q),$$

with respect to the generator, we have to compute $\frac{\partial \mathcal{L}}{\partial (\mu_P - \mu_Q)}$ that becomes

$$\frac{\partial \mathcal{L}}{\partial (\mu_P - \mu_Q)} = (I + 2A)(\mu_P - \mu_Q),$$

instead of

$$\frac{\partial \mathcal{L}}{\partial (\mu_P - \mu_Q)} = I(\mu_P - \mu_Q),$$

meaning that the gradients are scaled by $2A$. Since $\{\mathbf{v}_j\}_{j=1}^J$ are trainable, we can say that at each iteration of the generator, the gradients are altered by the matrix A whose eigen vectors are the directions in which P and Q are most different.

D. More on the Issue of Vanishing Gradient

In this section, we elaborate more on the idea of (Sajjadi et al., 2018) to emphasize more on the importance of the latent space of Auto-GLOCAD. They proposed to pass the data distribution through an autoencoder and use the reconstructed data as the target distribution for a generator. This might lead to instability in higher dimensions according to the following reasoning.

It was proved by Arjovsky & Bottou (2017, Theorems 2.1 and 2.2) that if $P_{\mathbf{X}}$ (real data) and $Q_{\mathbf{Y}}$ (fake data) have supports contained on two disjoint compact subsets, there is a smooth optimal discriminator that has perfect accuracy on the union of their supports. This results in a vanishing gradient issue for the generator that leads to instability (Arjovsky & Bottou, 2017, Theorems 2.4 and 2.6) because of two reasons:

- The data distribution naturally lives on a low-dimensional manifold.
- The generated distribution is the result of applying function $G : \mathbb{R}^{d_z} \rightarrow \mathbb{R}^{d_x}$ on random noise $z \in \mathcal{Z}$.

Arjovsky & Bottou (2017, Lemma 1) also proved that the $\dim(\text{Img}(G)) \leq \dim(\mathcal{Z})$ where $\dim(\cdot)$ denotes the manifold dimension. Now assume an autoencoder function with latent dimension l as $f_d(f_e(\cdot))$ where $f_e : \mathbb{R}^{d_x} \rightarrow \mathbb{R}^{d_l}$ and $f_d : \mathbb{R}^{d_l} \rightarrow \mathbb{R}^{d_x}$. Based on (Arjovsky & Bottou, 2017, Lemma 1), $\dim(\text{Img}(f_d \circ f_e)) \leq l$ where we normally have $l \ll d_x$ in autoencoders. This makes the real and fake data manifolds even more distinguishable and exacerbates the vanishing gradient problem. Simply speaking, lower-dimensional manifolds are more easily distinguishable in a high-dimensional embedding space. As a mental experiment, in a 3-dimensional embedding space, an imaginary discriminator has easier job when it discriminates two lines(1D manifold) than when it discriminates two planes(2D manifold).

In addition to stability issues, Mehrjou & Schölkopf (2018) showed that the entangled dynamics of (Sajjadi et al., 2018) may result in converging to a spurious equilibrium that can be avoided by making the dynamics disentangled that run with different timescales (Mehrjou et al., 2017).

E. Experiments

In this section, we provide details for the experiments presented in the main text and also present one more high-dimensional experiment that was eliminated from the main text due to the shortage of space.

E.1. Experiment Details

In this section, we provide the details of each experiment in Section. 4 of the text. The experiments of Section. 4.1 were numerical simulation of the differential equations which were derived analytically. The details of each experiment were mentioned in the text so we don't elaborate more on it here.

The experiment details for the 2-dimensional example of Section. 4.2 is as follows:

- Generator architecture: [Linear(512):Tanh:Linear(2048):Tanh:Linear(512):Tanh:Linear(256):Tanh:Linear(256)] with 10-dimensional input noise dimension.
- Kernel: Gaussian kernel with trainable bandwidth.
- Batchsize: 64
- Trade-off weight between MMD and UME term (λ): 0.1
- Learning rate for the generator, and witness points: 0.001
- The number of iterations each component is trained (n_g, n_v): 1
- Number of witness points: 20
- Convergence criterion: The magnitude of the gradients back propagated to witness points is less than a threshold ($1e - 5$) or the number of epochs is less than 20.

The experiment details for the MNIST and CIFAR10 examples are as follows

- Generator architecture:
[ConvTranspose2d(1024, 512, 4, 2, 1):BatchNorm(512):ReLU
:ConvTranspose2d(512, 256, 4, 2, 1):BatchNorm(256):ReLU
:ConvTranspose2d(256, 128, 4, 2, 1):BatchNorm(128):ReLU
:ConvTranspose2d(128, 1, 4, 2, 1):Tanh] with 100-dimensional noise in the input.
- Autoencoder architecture:

Encoder:[Conv2d(1, 64, 4, 2, 1):LeakyReLU(0.2)
:Conv2d(64, 128, 4, 2, 1):BatchNorm(128):LeakyReLU(0.2)
:Conv2d(128, 128, 4, 2, 1):BatchNorm(128):LeakyReLU(0.2,)]
Decoder:[ConvTranspose2d(hidden_dim, 128, 4, 2, 1):BatchNorm(128):LeakyReLU(0.2)
:ConvTranspose2d(128, 64, 4, 2, 1):BatchNorm(64):LeakyReLU(0.2)
:ConvTranspose2d(64, 1, 4, 2, 1):BatchNorm(1):Tanh()]

Notice that the first two arguments of Conv2d and ConvTranspose2d are the number of input and output layers. The last three arguments are kernel size, stride and padding respectively.

- Batchsize: 64
- Trade-off weight between MMD and UME term, $\lambda = 0.5$
- Number of witness points: 256
- Learning rate for the generator, encoder, decoder and witness points: 0.001
- The number of iterations each component is trained (n_g, n_e, n_d, n_v) : 1
- Kernel: inverse multi-quadratic $k(x, y) = (c^2 + \|x - y\|^2)^b$ with $c = 1.0$ and $b = -0.5$.
- Convergence criterion: The magnitude of the gradients back propagated to witness points is less than a threshold $(1e - 5)$ or the number of epochs is less than 20.

E.2. More Experiments

In this section, we present more experiments which were left out due to the shortage of space in the body of the text. As a follow-up to MNIST experiment, Fig. 9 and Fig. 10 show the progress of witness points and generated samples during the course of training for CIFAR10 dataset. Here, the whole set of witness points were initialized to samples from the training set. As can be seen, initially in the training process, the witness points show clear images suggesting that the generated distribution Q_Y is far from the data distribution P_X . As the training process goes on, the generated distribution captures the main structure of the data distribution and witness points become more and more unstructured suggesting that the difference between P_X and Q_Y is due to finer details. Notice that we did not intend to compete with state-of-the-art GANs in terms of image quality because this is not the focus of this paper. Therefore, we did not do any extensive hyper-parameter search or using extremely small learning rate to improve the quality of the generated images and stayed with the most basic implementation of the used GAN (Energy-Based GAN in this case).



Figure 9. The witness points learned by Auto-GLOCAD using the architecture inspired from Energy-Based GAN (Zhao et al., 2016).

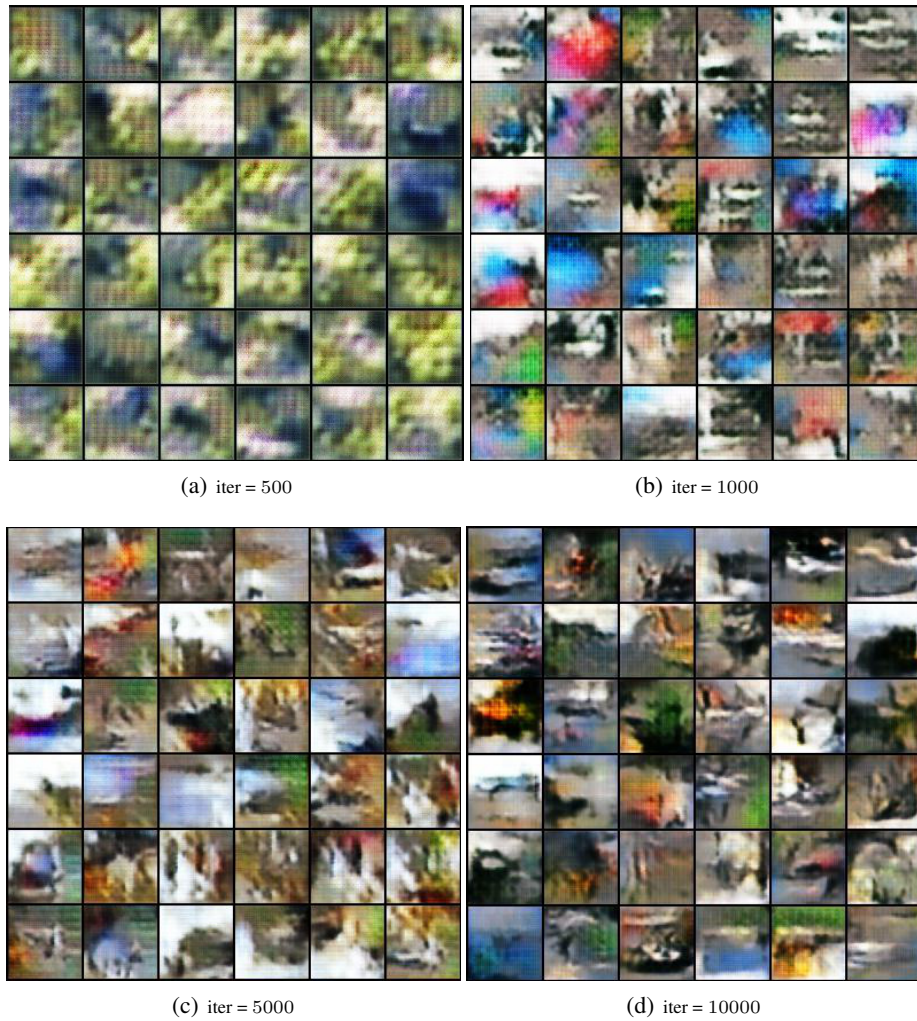


Figure 10. The generated samples learned by Auto-GLOCAD using the architecture inspired from Energy-Based GAN (Zhao et al., 2016).